Radiation Transport Analysis in Chalcogenide-Based Devices and a Neutron Howitzer Using MCNP

by

Herbert Bowler

A Thesis Presented in Partial Fulfillment
of the Requirements for the Degree
Master of Science

Approved October 2014 by the
Graduate Supervisory Committee:

Keith Holbert, Chair
Hugh Barnaby
Lawrence Clark

ARIZONA STATE UNIVERSITY

December 2014

ABSTRACT

As photons, electrons, and neutrons traverse a medium, they impart their energy in ways that are analytically difficult to describe. Monte Carlo methods provide valuable insight into understanding this behavior, especially when the radiation source or environment is too complex to simplify. This research investigates simulating various radiation sources using the Monte Carlo N-Particle (MCNP) transport code, characterizing their impact on various materials, and comparing the simulation results to general theory and measurements.

A total of five sources were of interest: two photon sources of different incident particle energies (3.83 eV and 1.25 MeV), two electron sources also of different energies (30 keV and 100 keV), and a californium-252 (Cf-252) spontaneous fission neutron source. Lateral and vertical programmable metallization cells (PMCs) were developed by other researchers for exposure to these photon and electron sources, so simplified PMC models were implemented in MCNP to estimate the doses and fluences. Dose rates measured around the neutron source and the predicted maximum activity of activation foils exposed to the neutrons were determined using MCNP and compared to experimental results obtained from gamma-ray spectroscopy.

The analytical fluence calculations for the photon and electron cases agreed with MCNP results, and differences are due to MCNP considering particle movements that hand calculations do not. Doses for the photon cases agreed between the analytical and simulated results, while the electron cases differed by a factor of up to 4.8. Physical dose rate measurements taken from the neutron source agreed with MCNP within the 10%

tolerance of the measurement device. The activity results had a percent error of up to 50%, which suggests a need to further evaluate the spectroscopy setup.

ACKNOWLEDGMENTS

I would like to express my deepest gratitude to Dr. Keith E. Holbert whose guidance and support made it possible for me to experience graduate school and learn about this topic.

I am grateful to committee member Dr. Hugh Barnaby for always remaining enthusiastic about my research and never failing to provide new ideas to explore. I would like to thank committee member Dr. Lawrence Clark for his support in the creation of my thesis.

I am thankful for all of Dr. Yago Gonzalez-Velo's help in ensuring that I understood aspects of my research that started off as a complete mystery to me. I am thankful to Blake Anderson for contributing a portion to my thesis and for his full support as both a colleague and a friend.

Finally, my sincerest thanks go to my friends and family for their undying support since the beginning.

TABLE OF CONTENTS

Page

CHAPTER Page

LIST OF TABLES

Table Page

Table Page

LIST OF FIGURES

Figure Page

Figure Page

1 INTRODUCTION

The Monte Carlo method was first formally described by applied mathematician and physicist John von Neumann in a 1947 letter to the theoretical division of Los Alamos National Laboratory (LANL) [1]. The example Neumann cited was that of a fissionable material and using statistics to decide the actions of neutrons as they travel through the material. When enough particle histories are considered, “a statistically valid picture is generated” [1]. This simple description forms the basis of one of most powerful nuclear analysis tools available to researchers today. What started as a suggestion from a passionate mathematician to LANL nearly seven decades ago has been extensively researched and developed into the Monte Carlo N-Particle (MCNP) transport code currently being used internationally.

MCNP has seen widespread use in developing simulation models of research reactors like the TRIGA Mark II and comparing simulated results with experimental reactivity to great accuracy [2]. As the need for innovation and safety arises, researchers are using MCNP to analyze the performance of new Generation IV reactor designs such as the supercritical water reactor before their expected viability in 2030 [3-4]. Radiation safety is also a concern for those who are interested in naturally occurring radioactive material (NORM) sources found in soil [5] and for those in the medical field researching californium-252 brachytherapy as a method of combating cancer [6].

Researchers at Arizona State University are currently exploring the capabilities of devices constructed out of a chalcogenide (ChG) glass. Chalcogenides are materials composed of elements from group 16 of the periodic table, and in particular, the chalcogens sulfur, selenium, and tellurium. The chalcogens are combined with certain

elements like germanium or arsenic in varying proportions to produce semiconductors with different physical properties.

An area of particular interest is the diffusion of surface metal atoms such as silver into the ChG glass by way of radiation exposure, which alters the electronic aspects of the glass. When Ag atoms diffuse into the ChG using light, the ChG is said to have been photodoped. This property is the driving mechanism behind programmable metallization cell (PMC) memory. The photodoped ChG serves as the electrolyte in these types of devices, where changes in the applied voltage cause the Ag to oxidize and form mobile Ag^+ ions. Under forward bias, these Ag^+ ions drift toward the cathode, which results in a decrease of resistance—the writing state. When a reverse bias is applied, the ions drift away from the cathode, which erases the device into a high-resistance state. Research [7] indicates that PMC devices have the potential to be used in radiation-intensive environments due to being relatively insensitive to radiation compared to charge-based memory devices. This “rad-hard” property of ChG-based PMCs has prospects of being implemented in space-based machinery.

Outer space as a radiation source is difficult to utilize for experimentation purposes, so radiation sources closer to home are employed in its place. Ionizing effects due to gamma rays are studied using irradiation units composed of radioactive cobalt-60 or cesium-137. For lower-energy photons, an ultraviolet light source or a copper K-alpha X-ray diffraction setup could be used. Electron accelerators are used to generate monoenergetic e-beams when beta radiation is being studied. Many fissionable isotopes, such as uranium-235 and plutonium-239 used in nuclear reactors, along with spontaneous

fission sources like californium-252 are used in testing environments that supply neutron irradiation.

As long as the user correctly and accurately defines the simulated world geometries, material compositions, and source specifications, materials in any radiation environment can be analyzed just as accurately. This research aims to demonstrate the agreements between radiation analysis results obtained in MCNP and compare them to simpler analytical models, and when possible, measurements.

This thesis is organized as follows: Chapter 2 outlines the MCNP methodology, the radiation sources considered and their simplifications as modeled in MCNP, and the particle interaction processes which are relevant in the analyses performed along with the theory which involves them; Chapter 3 describes the geometry of the devices subjected to photon and electron testing and explains how electron-hole pair generation constants can be determined in the photon cases; Chapter 4 uses the theory developed in Chapter 2 and compares the analytical results to those obtained in MCNP, along with explanations as to why the two might differ; Chapter 5 shifts the discussion toward ASU's Cf-252 neutron source, describing what the major functional goals were during its construction and how well its performance meets those goals, how its gamma-ray and neutron spectra were determined, how closely the simulated model matches manufacturer specifications and the reasons for any mismatch, and how MCNP can be used to determine the radioactivity of activation foils which are then compared to experimental values; and Chapter 6 summarizes the results of the research and how it could be expanded upon.

2 RADIATION TRANSPORT MODELING

This chapter provides an overview of the various radiation sources that were simulated in MCNP along with a description of the relevant physical theory and equations which provide a comparison between analytical and simulated results.

A. Monte Carlo Method

There are two major computation methods used to simulate an experiment and obtain a solution or value: deterministic and stochastic. Deterministic methods reach a solution by solving a transport equation based on the average particle behavior. For a particular set of inputs, a unique output is produced because it is assumed that particle behavior can be described exactly by an equation. In contrast, stochastic methods do not rely on transport equations and instead solve problems by simulating individual particles whose behaviors are described by probabilities and tallying certain aspects of their histories. MCNP, which stands for Monte Carlo N-Particle transport code, is an example of a stochastic method [8].

Los Alamos National Laboratory developed the MCNP code to model nuclear interactions between user-defined materials with a number of different particles in a three-dimensional universe. Until the introduction of MCNP6.1 in August 2013, the MCNP5 and MCNPX (for MCNP eXtended) packages were limited to simulating neutron, photon, and electron transport. In addition to physical capabilities not present in the previous codes, such as low-energy photon and electron transport, the production release of MCNP6.1 can now simulate protons, heavy ions, and even spontaneous fission sources.

MCNP tracks individual source particles as they traverse space, recording their interactions and determining a tally result based on statistical probabilities in the form of tabulated data. Table 2.1 shows the types of tallies available in MCNP. Each tally output is normalized per source particle. Multiplying a tally result by the number of source particles provides a direct quantity, but multiplying by the particle emission rate produces a flux instead of a fluence and a dose rate in place of a dose.

Table 2.1. Tally Categories Available in the MCNP Code

Tally Type	Description	Units
F1	Surface current	particles
F2	Surface fluence	particles/cm^2
F4	Fluence averaged over a cell	particles/cm^2
F5	Fluence at a point or ring detector	particles/cm^2
F6	Energy deposition	MeV/g
F7	Fission energy deposition	MeV/g
F8	Pulse height tally	pulses

A tally result is deemed acceptable if it passes all ten of the MCNP statistical checks which are related to the mean, the relative error *R*, the variance of the variance *VOV*, the figure of merit *FOM*, and the slope of the history scores [8]. Further, it is considered favorable to have a relative error as low as possible ($R < 0.05$), which is usually, though not always, related to simulating a greater number of source particles. In some cases, the value of *R* cannot be minimized within a reasonable timeframe; in this work, simulations lasting a week would occasionally not produce a result with a relative error below 0.08.

For this thesis, MCNP5 along with the beta and production versions of MCNP6 were used to obtain simulated data. Input decks were run on both software packages to

ensure that the version number did not significantly influence the end result. Low-energy photon transport was only modeled in MCNP6 due to its extended photon data libraries while the high-energy photons, electrons, and neutrons were simulated with both versions.

B. Radiation Sources

There were five radiation sources of interest in this research. The first is Arizona State University's Gammacell 220 radiation chamber, which uses rods of cobalt-60 to supply photons which bombard a sample. Each decay of a cobalt-60 atom emits two gamma rays with energies of 1.17 MeV and 1.33 MeV, whose average gamma-ray energy is 1.25 MeV. An ultraviolet (UV) photolithography tool which produces UV light with a wavelength of 324 nm and a corresponding photon energy of 3.83 eV is the second source. Two electron sources were considered: an electron beam source from Boise State University with an electron energy of 30 keV and an electron source of 100 keV. The last source considered was a neutron (and gamma) source utilizing californium-252.

In all cases but the neutron source, the simulated sources were simplified to have monodirectional and monoenergetic particles being emitted from a disk-shaped surface for the lateral devices and a square-shaped area for the vertical devices. The source shapes used in these simulations were chosen because they ensured that all of the MCNP statistical checks were passed. This should not imply that a unique source geometry is required to pass the statistics; factors like number of source particles and cell importance can also play a role. When the projected area of the source is greater than the cross-sectional area of a cell, as in the case of the disk-shaped sources, the particle fluence through the cell surface appears to be higher than it actually is. The effect of the radiation

source shape from the MCNP simulations can be eliminated by multiplying the result by a normalization factor of the two areas or by introducing a source weight in the simulation that is equal to the same factor. The monodirectional aspect was chosen for the Co-60 case because the highly penetrating gamma rays will traverse most materials without significant attenuation. Although not strictly accurate, the fact that the light source of the UV photolithography machine is positioned relatively far from the sample compared to the sample dimensions justifies an approximately monodirectional assumption. The electrons strike a sample as a collimated beam which is clearly monodirectional. The dimensions of the actual Cf-252 source were taken into consideration in the MCNP model, where neutrons and gamma rays were emitted from a volumetric, isotropic cylindrical cell.

C. Radiation Interaction Processes

As radiation particles travel through a medium, they interact with nuclei or electrons through interactive processes which are detailed in this section.

1) Photons

A photon is a quantum of light characterized by its neutral charge and zero rest mass. Photon interactions with matter are characterized by an energy-dependent factor called the cross section. A microscopic cross section, denoted by the symbol σ_i for the *i-th* reaction type, has a unit of area/atom and represents the effective cross-sectional area of a nucleus. The typical unit for cross sectional area is a barn, which is equivalent to 10^{-24} cm^2. The larger the microscopic cross section, the greater the chance that an interaction will take place. The attenuation (or linear) coefficient μ_i can be obtained from the microscopic cross section by the following relation:

$$\mu_i = N\sigma_i \tag{1}$$

where N is the atom density of the material. The attenuation coefficient μ_i represents the probability of an i-type interaction occurring per unit length that a photon travels through a medium. Related to the attenuation coefficient is the mass attenuation (or interaction) coefficient μ/ρ, which is equal to

$$\frac{\mu}{\rho} = \frac{N\sigma_{tot}}{\rho} \tag{2}$$

where σ_{tot} is the total cross section for an atom at a particular energy and ρ is the density of the material. Note that σ_{tot} could be essentially equal to one cross section if it is dominant at that energy. This value describes the probability of any photon interaction occurring per unit mass. For a particular photon interaction, Equation (1) can also be divided by the material density to determine the mass interaction coefficient μ_i/ρ of an i-type reaction. Finally, a value termed the mass-energy absorption coefficient μ_{en}/ρ is determined from the transfer of the kinetic energy of a source photon E_p to charged particles in a medium using the various photon interactions [9]. The determination of this value is rather involved, but data tables exist which tabulate μ_{en}/ρ for elements up to uranium [9]. Using the mass-energy absorption coefficient, the external photon dose can be determined according to:

$$D = \Phi E_p \left(\frac{\mu_{en}}{\rho} \right) \tag{3}$$

where Φ is the photon fluence, or the number of source particles S flowing through an area A:

$$\Phi = \frac{S}{A}. \tag{4}$$

Because MCNP normalizes each result per source particle, in Equation (4), $S = 1$.

The photon interaction data tables in MCNP account for three major interaction mechanisms: the photoelectric effect, Compton scattering, and electron/position pair production. These data sets are used in conjunction with form factor, scattering function, and other data to enable a more complete photon analysis [8]. The photoelectric effect dominates at low photon energies while the Compton and pair production effects dictate the intermediate and high energy ranges, respectively [10].

a) Photoelectric Effect

The photoelectric effect takes place when an impinging photon above a certain threshold frequency interacts with and is absorbed by an atom, which releases a photoelectron. These electrons are usually emitted from the *K* shell of the atom, which is closest to the nucleus. Because the recoiling atom is significantly more massive than the electron, nearly all of the photon energy E_p is transferred to releasing the electron from the atom with binding energy E_b and ejecting it with a kinetic energy E_e according to

$$E_e = E_p - E_b. \tag{5}$$

As the number of protons *Z* in a nucleus increases, the binding energy of the *K*-shell electron increases from a few eV to around 100 keV, which is where the photoelectric effect dominates.

b) Compton Scattering

Compton scattering takes place when the incident photon is deflected by a free electron and is not absorbed by the atom. After scattering at an angle of θ_s the photon has a kinetic energy equal to

$$E_p^{'} = \frac{E_p}{1+[E_p/(m_e c^2)](1-\cos\theta_s)} \tag{6}$$

where m_e is the rest mass of an electron and c is the speed of light. Coherent scattering, also known as Rayleigh scattering, takes place when the incoming photon maintains most of its energy and original trajectory. Incoherent, or Raman scattering occurs when E_e is comparable to E_b. The Compton scattering cross section decreases with increasing photon energy.

c) Pair Production

At higher photon energies, the incident photon is absorbed by the atom and creates an electron-positron pair. This interaction can occur when the photon has at least the rest-mass energy of the pair, and its cross section increases with higher energy.

2) Electrons

MCNP considers a wide number of electron transport processes, including Coulomb scattering, knock-on (also known as delta-ray) electrons, and the production of X-rays and bremsstrahlung. Coulomb scattering and collisional energy loss takes place as electrons travel through a medium, which ionizes the material and can cause excitation. Source electrons can collide with other electrons in the material and transfer a significant portion of their energy to them, which in turn could further ionize and excite atoms.

When these secondary electrons have enough energy to cause additional ionizations, they are known as knock-on electrons.

Relationships exist that relate the energy of a beta particle, which is an electron emitted from a decay action, to its maximum range $R_{\max}$. The electrons considered in this research were not technically beta particles, but electrons behave identically whether or not their source was radioactive. Therefore, the material-independent Katz-Penfold relation [11] is assumed to hold for primary electrons and is defined as

$$R_{\max}\ [\mathrm{g/cm^2}] = \begin{cases} 0.412E_0^{\,1.265-0.0954\ln(E_0)} & 0.01 \le E_0 \le 2.5\ \mathrm{MeV} \\ 0.530E_0 - 0.106 & E_0 > 2.5\ \mathrm{MeV} \end{cases} \tag{7}$$

where E_0 is the incident electron energy in MeV. The maximum range can then be used to determine the thickness of material needed to completely stop an electron, which is called the penetration depth t_d:

$$t_d = \frac{R_{\max}}{\rho}. \tag{8}$$

The linear energy transfer *LET* is the amount of energy that a beta particle loses and transfers to a material per unit length as it traverses the material. It is assumed to have a linear relationship and can be determined using

$$LET = \frac{E_0}{t_d}. \tag{9}$$

Therefore, the total change in beta particle energy ΔE from when it enters a material of thickness t to when it exits with a final energy E_f is simply

$$\Delta E = E_0 - E_f = (LET)(t). \tag{10}$$

Using Equation (8) and Equation (10), the absorbed electron dose D can be defined:

$$D = \frac{\Delta E}{\rho\, t\, A_{dev}} \tag{11}$$

where A_{dev} is the cross-sectional area of the device upon which the source is projected. After some rearranging, it can also be shown that the absorbed electron dose has a simplified result which does not depend on density or material thickness:

$$D = \frac{E_0}{R_{\max} A_{dev}}. \tag{12}$$

Electron doses determined using Equation (12) assume that the electrons transfer all of their energy into a material which is only true if $t \geq t_d$. PMC layers are generally too thin to meet this requirement, so Equation (11) was used instead to determine the electron dose since it accounts for how much electron energy is actually transferred to each layer.

3) Neutrons

Neutrons have no net charge, and as a result, their interactions with an atom are mostly limited to the nucleus. In much the same way as photons, their interaction probabilities are also characterized by microscopic cross sections in units of barns/atom. Contrary to the photon macroscopic cross section μ_i, the neutron macroscopic cross section for the *i-th* reaction is denoted by the symbol Σ_i.

Nuclear reactions can be generalized by the following equation:

$$a + b \rightarrow c + d \tag{13}$$

where *a* and *b* represent the initial nuclei or particles and *c* and *d* represent the products. If the incident particle *a* strikes a nucleus *b*, a resultant nucleus *c* and an emitted particle *d*

are produced. The emitted particle may or may not be the same as the incident particle. Equation (13) can then be restated using a different notation:

$$b(a,d)c\ . \tag{14}$$

It is the parenthetical term of Equation (14) which indicates the type of neutron reaction that occurs.

Most of the neutron interaction processes can be categorized as either a scattering or an absorption reaction. In a scattering event, a neutron strikes a nucleus and reappears after the collision. If the nucleus remains in its ground state, an elastic collision of the form (n,n) has taken place. When the nucleus enters an excited state upon being struck by a neutron, an inelastic collision (n,n') takes place, where the prime notation indicates that the neutron is scattered with a noticeably lower energy. The excited nucleus then decays by releasing gamma rays. The elastic and inelastic cross sections are denoted by the subscripts *e* and *i*, respectively [12].

As its name implies, absorption reactions take place when the neutron is absorbed by the nucleus instead of scattered. Radiative capture takes place when the nucleus absorbs a neutron and subsequently releases a gamma ray, denoted by (n,γ). Neutrons can also be released from the nucleus of atoms, resulting in a particle production reaction whose notation is (n,2n) in the case when a single net neutron is released from the nucleus, (n,3n) for when two neutrons are released, and so on. Charged particles such as protons can also be ejected, which is denoted by (n,p) for proton production or (n,α) for an alpha particle, which is a helium nucleus, or two protons bound to two neutrons. The cross sections are denoted according to the ejected particle.

3 PMC DEVICE AND MATERIAL SPECIFICATIONS

Programmable metallization cells have two basic forms: lateral or vertical. The direction that the mobile ions flow determines whether the device is considered lateral or vertical. In a lateral device, the electrodes are coplanar, which causes mobile ions to drift along the thin layer. Due to the low cross-sectional area through which electrons flow, these types of devices are better suited for applications which require low capacitance. Vertical devices position the solid electrolyte between the two electrodes, which causes the current to flow vertically. Because electrons only have to travel a short distance between electrodes, these devices excel in producing fast-switching resistive memory.

Both types of devices were of interest in this research, although only the parameters directly related to radiation and not the various electrical properties were studied here. In this chapter, the types of devices used in the photon and electron MCNP simulations will be described.

A. Lateral Device

Figure 3.1 shows an overhead view of the lateral device developed by the research team. This structure is layered with Ag, the non-photodoped chalcogenide, SiO_2, and bulk Si. Nickel contacts were deposited on top of the Ag layer. The lateral device is to be used as a radiation sensor where the Ag provides a low-resistance electrical pathway between the two Ni contacts whose resistance increases as the Ag photo-diffuses into the ChG upon being exposed to gamma-ray radiation [13]. The composition of the ChG analyzed in the radiation effects experiments was $Ge_{30}Se_{70}$. The dimensions of the lateral device were inferred from Figure 3.1 and were found to be 308 μm by 184.8 μm. The Ag layer is situated closest to the radiation source. Figure 3.2 shows a diagram of the device cross

section along with the layer thicknesses. The Ni contacts were not modeled as the materials of interest were the Ag and ChG.

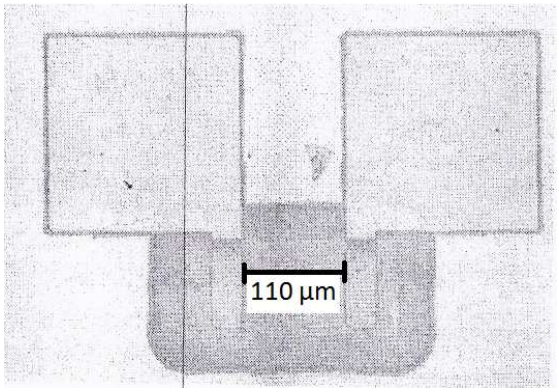

Figure 3.1. Lateral Device Developed by the Research Team

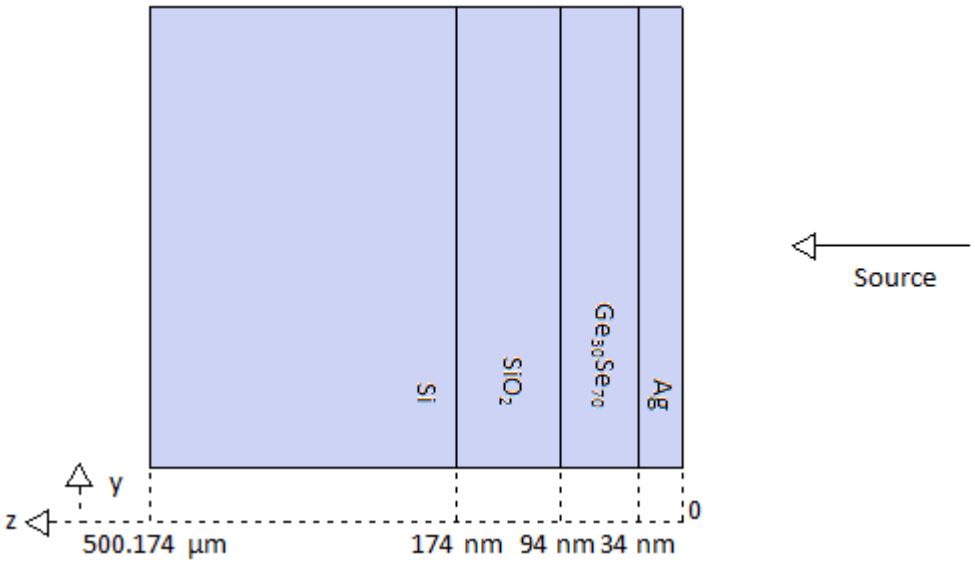

Figure 3.2. Cross Section of the Lateral Device

In order to analyze the effect of depth on the dose and fluence, each layer was divided into multiple cells in the MCNP simulation. The ChG layer was split into ten

equal cells, each with a thickness of 6 nm. The non-ChG layers were split into five cells per material; that is, each Ag cell had a thickness of 6.8 nm, each SiO_2 cell had a thickness of 16 nm, and the Si cells each had a thickness of 100 μm. The monodirectional source was chosen to have a radius of 182 μm, which is larger than the projection of the device. The device and the source were enclosed in a cylindrical world just larger than the source. These geometries were chosen in order to pass the ten statistical checks. Tallies measuring surface fluence at each interface in particles/cm^2 and the dose in MeV/g were obtained. The MCNP results are normalized per source particle.

B. Vertical Device

Figure 3.3 shows the geometry of the thin-film vertical device. This structure is layered with Ag, $Ge_{30}Se_{70}$ photodoped with an atom percentage of Ag ranging from 0% to 30%, Ni, SiO_2, and bulk Si. The depth of the Ag layer was taken to be 35 nm, the depth of the Ag-ChG layer was 60 nm, and the width and height were taken to be 2.5 μm. The Al anode and cathode extend across the face of the structure and are up to 300 nm in length and width. As with the lateral device, the Ag layer is situated closest to the source.

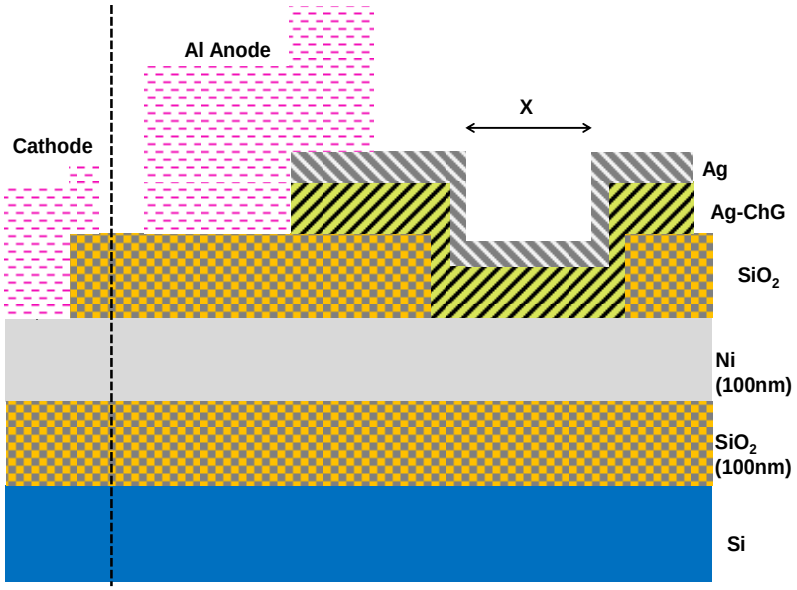

Figure 3.3. Diagram of the Vertical Structure

Both the SiO_2 layer and the Si layer were neglected in modeling the structure in MCNP. Neglecting the SiO_2 and Si layers was acceptable as the materials of interest were the Ag and ChG layers. The Al cathode and anode were also not modeled. The Ni layer was included in the model because particles may backscatter from the Ni layer back into the ChG layer. The simplified model, which is the active area of the device within the boundaries of "*x*" labeled in Figure 3.3, is shown in Figure 3.4.

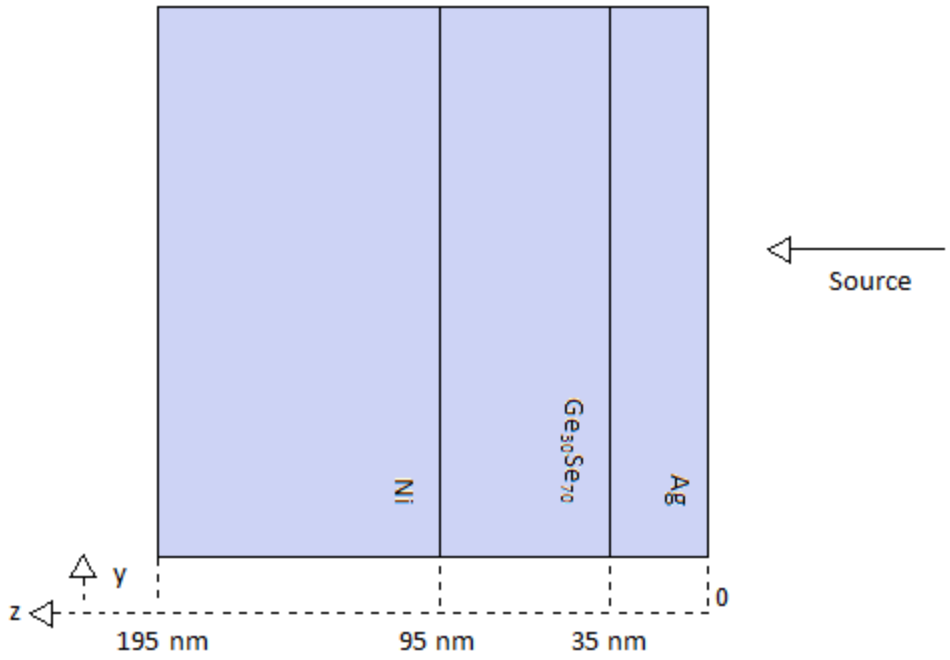

Figure 3.4. Simplified Vertical Structure Modeled in MCNP

As with the lateral device, the non-ChG layers were split into five cells per material, so each Ag cell had a thickness of 7 nm and each Ni layer had a thickness of 20 nm. The ChG layer was split into ten cells, each 6 nm thick. Unlike the source used in the lateral device simulations, the source modeled for the vertical devices had the same area as the device face which also allowed the results to pass the statistical checks.

It is readily observed in Figure 3.2 and Figure 3.4 that the simulated models are quite similar. However, the differences in the physical geometry between the devices influence various electrical properties and not the parameters of interest here, which are the energy deposition per material and the particle fluence. The simplified models were therefore deemed sufficiently instructive.

C. Device Materials

Table 3.1 lists various properties of the elements used within the devices. Atomic numbers and atomic weights were taken from [14]. Material densities and mass-energy attenuation coefficients were taken from [9]. Figure 3.5, Figure 3.6, Figure 3.7, Figure 3.8, Figure 3.9, and Figure 3.10 show cross section data for each element in order of increasing atomic number, which were obtained from the Evaluated Photon Data Library (EPDL) [15]. The cross sections shown are coherent (Rayleigh) scattering (CS), incoherent (Raman) scattering (IS), photoelectric effect (PE), pair production (PP), and triplet production (TP). At very low photon energies, below 5 eV, the CS reaction is shown to be dominant for each element.

Tabulated values of μ_{en}/ρ do not exist at the UV photon energy, so a value had to be determined. Unlike the mass attenuation coefficient μ/ρ, whose value could be approximated by considering only the dominant cross section at a particular energy, μ_{en}/ρ cannot be determined as easily. Regardless, when the CS cross section is used in the determination of μ/ρ, whose value was then used in Equation (3) in place of μ_{en}/ρ, the analytical results agreed well with the MCNP results in the UV source case. This makes little physical sense as the energy absorbed or deposited per collision is determined by the photoelectric effect, pair production, and incoherent scattering interactions and not on coherent scattering, where the photon is scattered with minimal energy loss [16]. The negligible kinetic energy transfer associated with coherent scattering explains why its contribution is omitted when determining μ_{en}/ρ [9]. It should be noted, however, that data regarding the energy transfer of coherently scattering photons at low UV energies are not widely available, and as a result, it is unclear as to how much energy deposition actually

occurs. That the CS interaction could be used to determine the dose shows either that MCNP does not analyze low-energy situations correctly or that μ_{en}/ρ is approximately equal to μ/ρ at low-energy situations. Proving the latter case is beyond the scope of this work. Performing low-energy dose calculations using the CS cross section provides insight into the limitations of MCNP.

Table 3.1. Atomic Properties of the Elements

Material	Atomic Number	Atomic Weight (amu)	Density (g/cm^3)	μ_{en}/ρ at 1.25 MeV (cm^2/g)	μ/ρ at 3.827 eV (cm^2/g)
O	8	16.00	1.33×10^{-3}	0.0267	8.72×10^{-3}
Si	14	28.09	2.33	0.0265	1.53×10^{-3}
Ni	28	58.69	8.91	0.0254	0.270
Ge	32	72.63	5.32	0.0235	1.19×10^{-4}
Se	34	78.96	4.82	0.0231	1.73×10^{-4}
Ag	47	107.87	10.49	0.0243	0.265

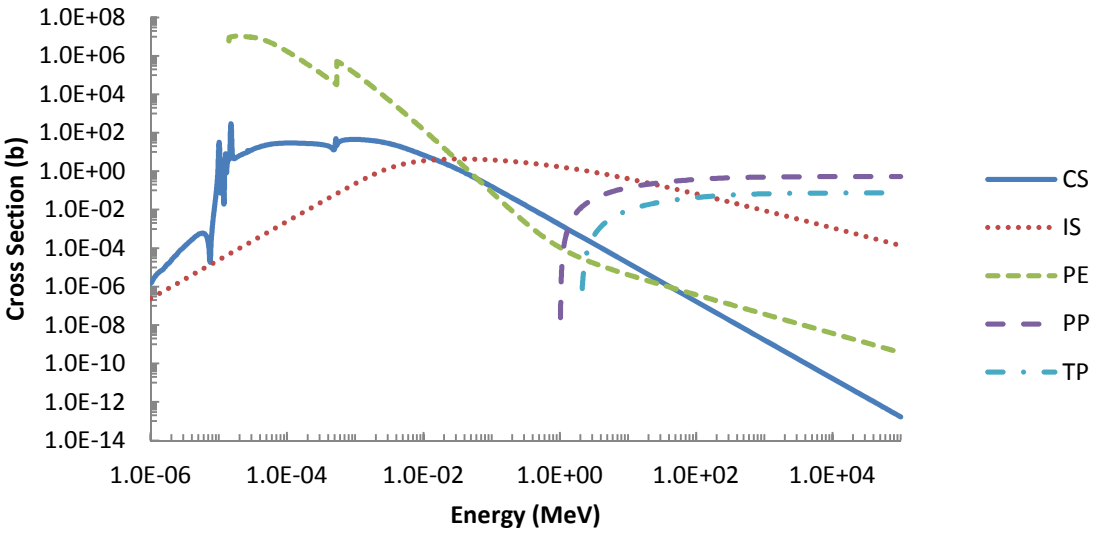

Figure 3.5. Oxygen Photon Cross Sections

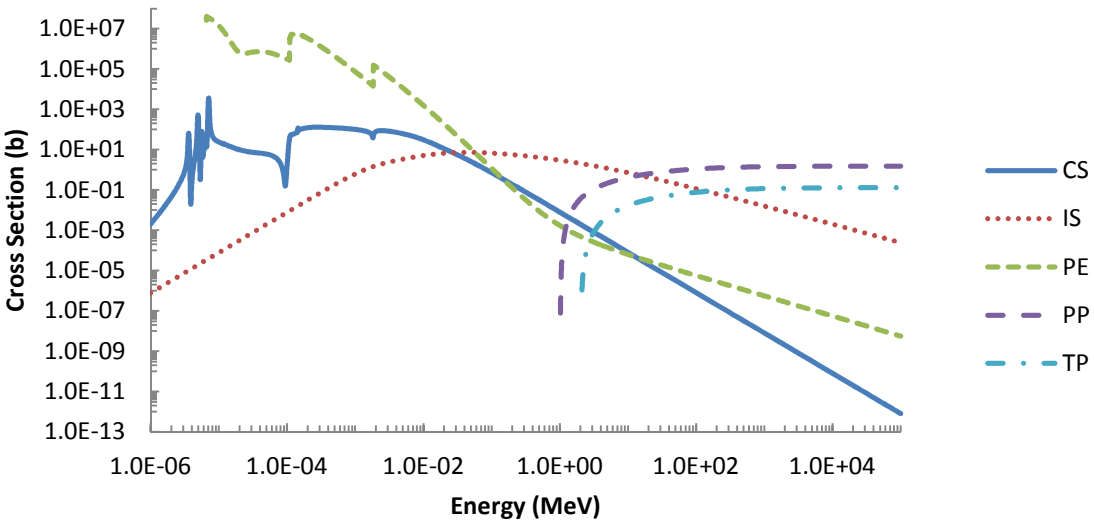

Figure 3.6. Silicon Photon Cross Sections

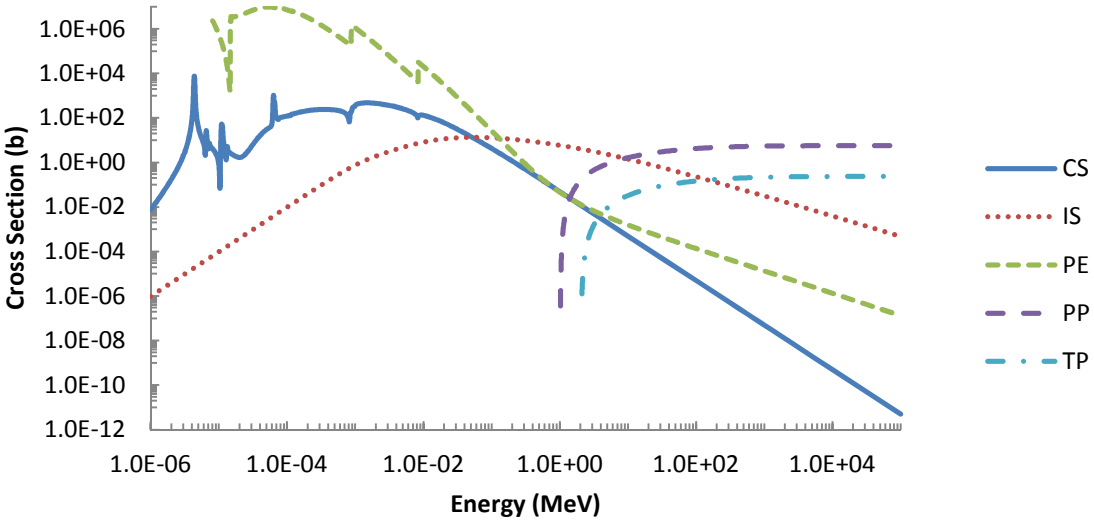

Figure 3.7. Nickel Photon Cross Sections

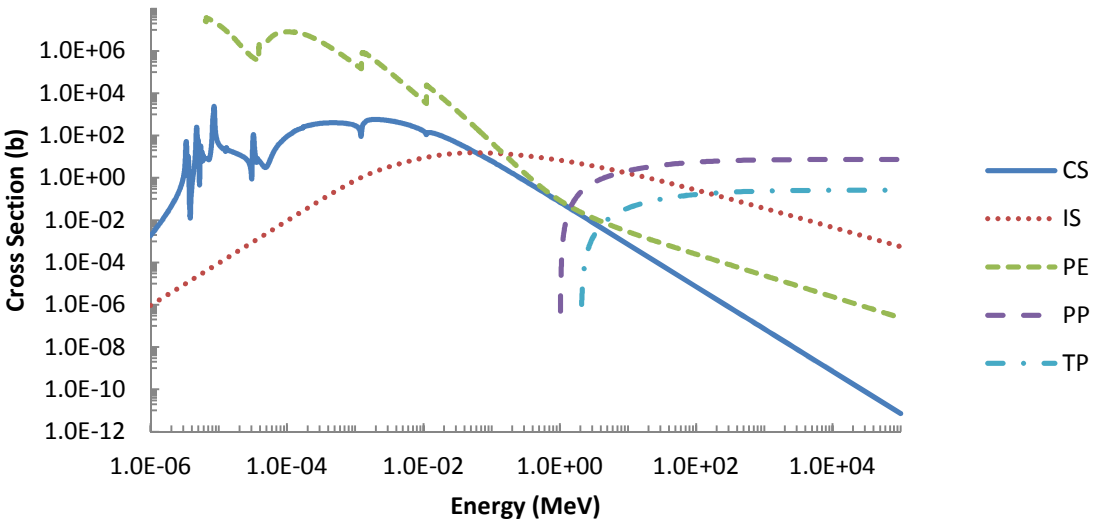

Figure 3.8. Germanium Photon Cross Sections

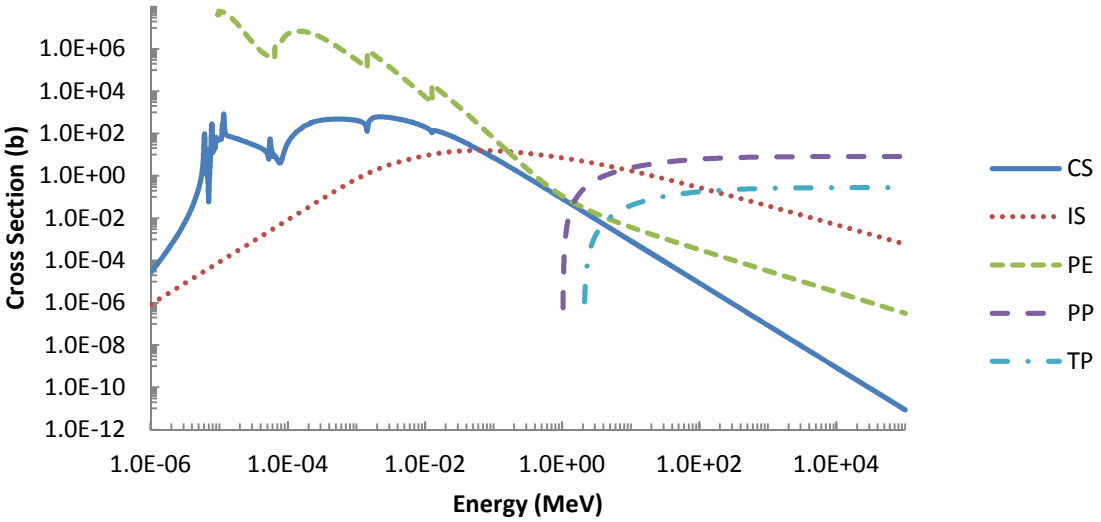

Figure 3.9. Selenium Photon Cross Sections

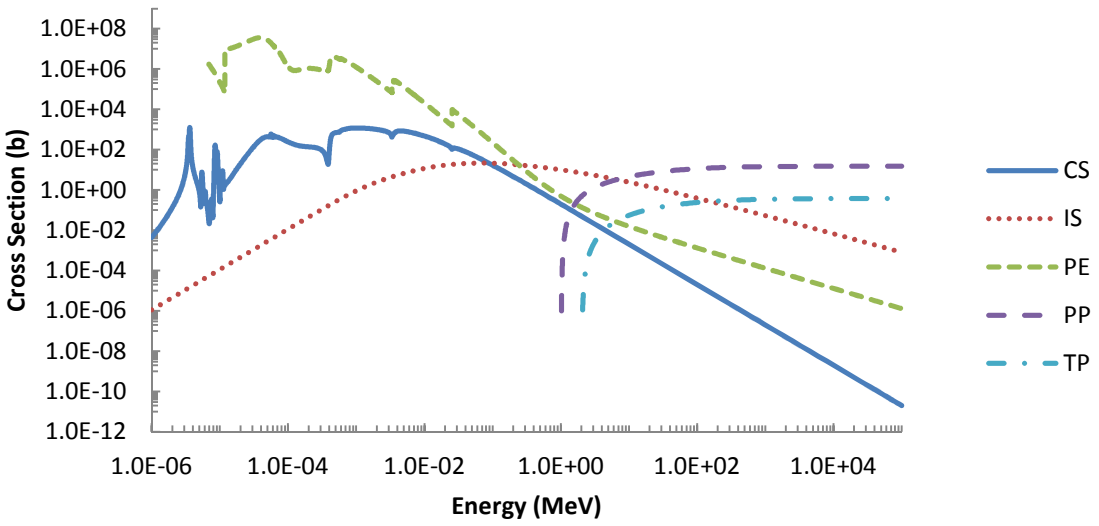

Figure 3.10. Silver Photon Cross Sections

The electron–hole pair (ehp) generation constant can be determined using

$$g_0 = \frac{\rho}{w_{ehp}} \approx \frac{\rho}{2.8E_{opt}} \tag{15}$$

where w_{ehp} is the electron-hole pair creation energy of the semiconductor and E_{opt} is the optical gap energy. The approximation $w_{ehp} \approx 2.8E_{opt}$ comes from an analysis by Alig and Bloom [17]. The density for the ChG layer was determined to be 4.8 g/cm^3 by a separate research team [18]. Starting with 0% Ag content in $Ag_x(Ge_{0.25}Se_{0.75})_{100-x}$, i.e., $x = 0$, using the E_{opt} values found in [19] leads to the generation constant values shown in Table 3.2. The values shown in Table 3.2 assume the ChG density does not change as it is photodoped.

Table 3.2. Generation Constant Calculations Assuming Density Does Not Change

Ag content x (%)	E_{opt} (eV)	g_0 [ehp/(rad·cm^3)]
0	2.06	5.20×10^{13}
7	1.88	5.70×10^{13}
10	1.79	5.99×10^{13}
20	1.64	6.53×10^{13}
25	1.55	6.91×10^{13}

As the ChG is photodoped, its density will increase as the Ag migrates [20]. Assuming that the volume of the material does not change as the photodoping amount increases, an estimate for the density increase in $Ag_x(Ge_{0.30}Se_{0.70})_{100-x}$ as the ChG is photodoped can be determined as shown below.

$$\begin{aligned} w_{Ge} &= \frac{0.30M_{Ge}}{0.30M_{Ge}+0.70M_{Se}} \\ &= \frac{(0.30)(72.61\text{ g/mole})}{(0.30)(72.61\text{ g/mole})+(0.70)(78.96\text{ g/mole})} = 0.283 \\ w_{Se} &= \frac{0.70M_{Se}}{0.30M_{Ge}+0.70M_{Se}} \\ &= \frac{(0.70)(78.96\text{ g/mole})}{(0.70)(78.96\text{ g/mole})+(0.30)(72.61\text{ g/mole})} = 0.717 \end{aligned} \tag{16}$$

where w is the weight fraction of the element and M is the molar mass of the element. For a 1 cm^3 sample of pure $Ge_{30}Se_{70}$, the total number of atoms is

$$\begin{aligned} n_{total} = n_{Ge}+n_{Se} &= (4.8\text{ g})\left[\frac{w_{Ge}}{M_{Ge}}+\frac{w_{Se}}{M_{Se}}\right]N_A \\ &= 3.75\times10^{22}\text{ atoms of Ge and Se} \end{aligned} \tag{17}$$

where N_A is Avogadro's number. The increase in the mass of the pure ChG sample is equivalent to the mass of Ag that diffuses into the ChG, which is calculated as

$$m_{Ag} = \frac{n_{total} M_{Ag}}{N_A} \frac{x}{100 - x} \tag{18}$$

where x is the atom percentage of Ag in the ChG. Using Equation (18) to determine the new densities of the ChG, the new generation constants were calculated and are shown in Table 3.3.

Table 3.3. Generation Constants Determined Using Estimated Density Values

Ag content x (%)	ρ (g/cm^3)	g_0 [ehp/(rad·cm^3)]
0	4.80	5.20×10^{13}
7	5.31	6.30×10^{13}
10	5.55	6.92×10^{13}
20	6.48	8.82×10^{13}
25	7.04	1.01×10^{14}

The assumption that the volume of the ChG layer does not increase as it is photodoped is not necessarily valid. When a thin-film ChG material is saturated with photo-diffused Ag, the resulting ternary could be 10% to 15% thicker than the binary from which it was formed assuming there is no horizontal ballooning of the material [21]. This means that the estimated density values in Table 3.3 could overestimate the actual densities by up to 15%. In the interest of producing generation constant plots with more than just the lower and upper bounds of the Ag concentration in the ChG, any thickness increase was neglected. For ChG glasses of the form Ge_aSe_{1-a}, where a ranges from 4% to 40%, the densities of all the glasses were found to be within 1% of each other [22]. Therefore, the estimated densities for $Ag_x(Ge_{0.30}Se_{0.70})_{100-x}$ are assumed to apply to any Ag-Ge-Se ternary of the form $Ag_x(Ge_aSe_{1-a})_{100-x}$. It should be noted that the density

reported in [18] is higher than those stated in [22], but because the former value was obtained more recently it was assumed to be valid in this research.

In the same manner as with $Ag_x(Ge_{0.25}Se_{0.75})_{100-x}$, the values of E_{opt} for $Ag_x(Ge_{0.20}Se_{0.80})_{100-x}$ given in [23], the estimated densities, and the generation constants with increasing Ag are shown in Table 3.4. Figure 3.11 shows a plot of the generation constant as a function of Ag concentration for the two ChG compositions considered.

Table 3.4. Generation Constants for Photodoped $Ge_{20}Se_{80}$

Ag content x (%)	E_{opt} (eV)	ρ (g/cm^3)	g_0 [ehp/(rad·cm^3)]
0	1.90	4.80	5.64×10^{13}
6	1.87	5.23	6.24×10^{13}
11	1.66	5.63	7.57×10^{13}
16	1.60	6.08	8.48×10^{13}
20	1.53	6.48	9.45×10^{13}
23	1.39	6.81	1.09×10^{14}

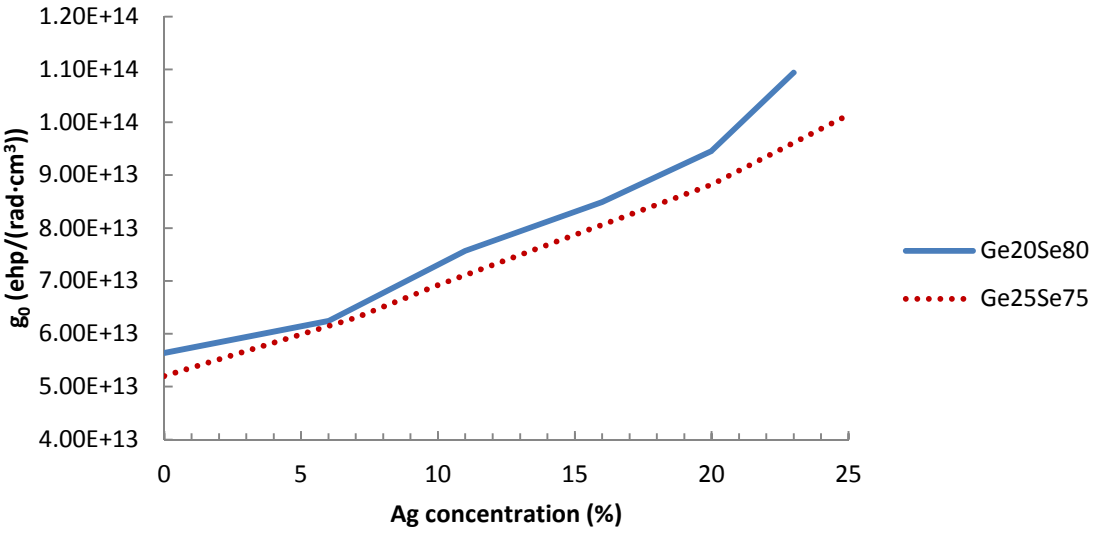

Figure 3.11. Estimated Generation Constants for Various Ge Concentrations

As shown in Figure 3.11, the generation constant increases with Ag concentration. This is due to the lower binding energy between Ag-Se bonds compared to the Ge-Se binding energy [23]. A lower binding energy means that less photon energy is required to excite a valence band electron into the conduction band which results in a decrease in the optical bandgap E_{opt}. Thus, the generation constant increases due to the inverse relationship with E_{opt}. It is also shown in Figure 3.11 that a higher chalcogen (Se) concentration leads to an increase in the generation constant because more Ag-Se bonds can be formed [24].

4 ANALYTICAL AND MCNP SIMULATION ANALYSES

This chapter will utilize the theory developed in Chapter 2, Section C to obtain analytical results. These values will then be compared to the results from MCNP simulations which model the geometry of the devices given in Chapter 3.

A. Lateral Device

1) Cobalt-60 Source

Using Equation (4) and a source radius of 0.0182 cm, the photon fluence for the lateral device is

$$\Phi = \frac{S}{A} = \frac{1 \text{ photon}}{\pi(1.82\times10^{-2} \text{ cm})^2} = 961 \text{ photons/cm}^2 . \tag{19}$$

The same geometry was implemented in MCNP for all of the photon and electron sources, so the value of the analytical fluence does not change. The mass-energy absorption coefficient for a mixture can be determined using

$$\frac{\mu_{en}}{\rho} = \sum_i w_i \left(\frac{\mu_{en}}{\rho}\right)_i \tag{20}$$

where w_i is the weight fraction of a material. For $Ge_{30}Se_{70}$, the weight fractions can be evaluated to give w_{Ge} = 0.2827 and w_{Se} = 0.7173. Using these weight fractions and the values of μ_{en}/ρ for Ge and Se, Equation (20) can be evaluated at a photon energy of 1.25 MeV as

$$\begin{aligned}\left(\frac{\mu_{en}}{\rho}\right)_{Ge_{30}Se_{70}} &= (0.2827)\left(2.353\times10^{-2}\,\frac{\text{cm}^2}{\text{g}}\right) + (0.7173)\left(2.306\times10^{-2}\,\frac{\text{cm}^2}{\text{g}}\right) \\ &= 2.319\times10^{-2}\,\frac{\text{cm}^2}{\text{g}}\end{aligned} \tag{21}$$

The dose can then be evaluated for the ChG:

$$D = \left(961 \frac{\text{particles}}{\text{cm}^2}\right)\left(1.25 \frac{\text{MeV}}{\text{particle}}\right)\left(2.319 \times 10^{-2} \frac{\text{cm}^2}{g}\right) = 27.9 \frac{\text{MeV}}{\text{g}}. \quad (22)$$

The doses for the other layers can be determined in a similar manner and the results can be seen in Table 4.1.

Table 4.1. Analytical Dose at E_p = 1.25 MeV for the Lateral Device per Source Photon

Material	μ_{en}/ρ (cm^2/g)	D (MeV/g)
Ag	2.43×10^{-2}	29.2
$Ge_{30}Se_{70}$	2.32×10^{-2}	27.9
SiO_2	2.68×10^{-2}	32.2
Si	2.65×10^{-2}	31.9

Figure 4.1 shows a plot of the fluence through the lateral structure as a function of depth, where SP stands for "source particle." The depth values were taken with respect to their distance away from the Ag surface closest to the source. Note that the first data point corresponding to the Air/Ag interface is 0 nm, which cannot be plotted on a logarithmic scale. As such, the Air/Ag interface was arbitrarily placed “to the left” of the data point corresponding to the start of the second cell into the Ag layer. Error bars were not included due to them being smaller than a plot marker. The analytical fluence is shown to be slightly greater than the fluence determined by MCNP. The MCNP simulations also show that the fluence decreases in the Si layer due to being much thicker than the other layers, but the high energy of the gamma rays makes this decrease very slight.

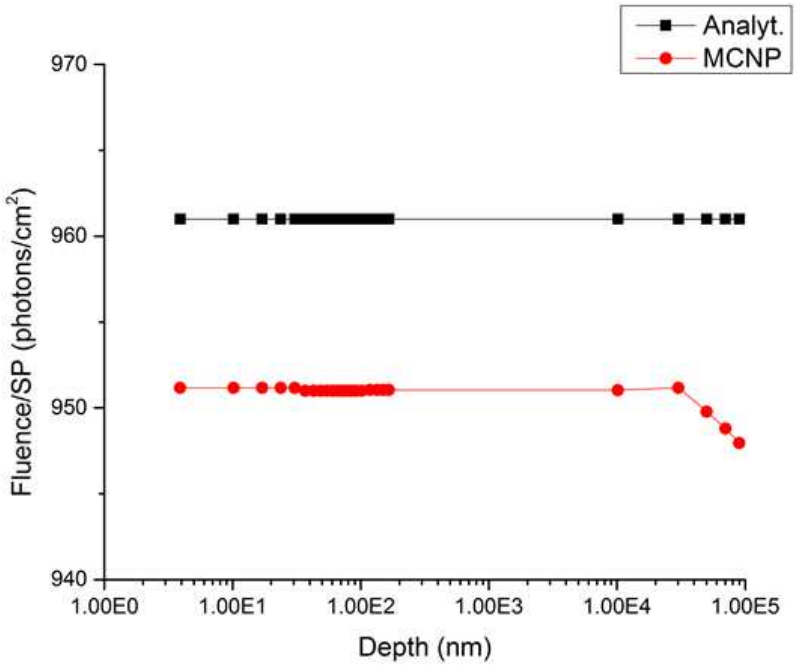

Figure 4.1. Fluence per Source Particle for Gamma Rays in the Lateral Device

Although Figure 4.1 depicts a sharper fluence decrease deep into the device in the Si layer, the amount changes by only 0.3%. The fluence, therefore, does not change significantly as a function of depth. This result was expected, as the attenuation factor for a material is equal to $e^{-\mu x}$, where μ is the total interaction coefficient of the material and x is the thickness. Because the thickness of each material is on the nanometer scale, the value of $e^{-\mu x}$ is very close to 1, meaning little attenuation takes place. The fluence decrease observed in the Si layer occurs due to it being thousands of times thicker than the other layers.

Figure 4.2 shows the gamma dose in each material versus depth. The depth values were taken to be the half the distance through a cell. The gamma dose depends primarily on the material and does not change significantly within a given material.

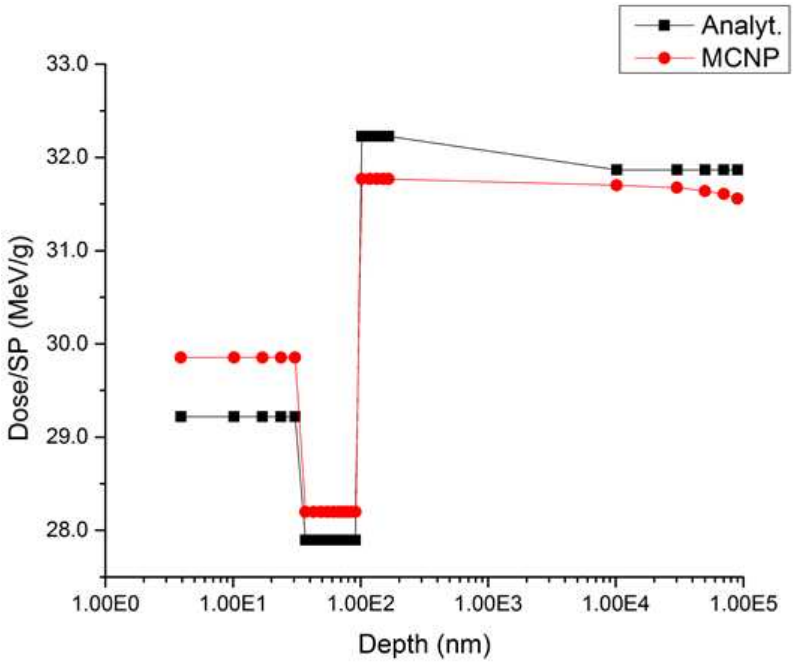

Figure 4.2. Gamma Dose per Source Photon in Lateral Device as a Function of Depth

Table 4.2 shows the results from the MCNP results and the percent error between the corresponding analytical calculations. The errors were low, which shows that the theory agrees well with MCNP simulations. It should be noted here that in these particular simulations, a relatively low amount of particles (80,000) were simulated in order for MCNP to pass all ten of its statistical checks. The stated tally errors for the fluences and the doses were approximately 0.1%. When the amount of particles is increased to 800,000, the simulation fails some statistical checks, but the fluence output becomes 961 photons/cm^2. This value better matches the analytical calculation. Although it is recommended that users run simulations which pass all ten of the MCNP statistical checks, this result could indicate that passing these checks comes with a cost of reduced tally output accuracy when the number of simulated particles is low. This should be kept

in mind with the remainder of the lateral device results, which were simulated with a similarly low amount of source particles.

Table 4.2. Comparison of Analytical and Simulated Gamma Fluence and Dose Values

Material	Fluence from MCNP (photons/cm^2)	Percent Error (%)	Dose from MCNP (MeV/g)	Percent Error (%)
Ag	951	1.0	29.9	2.2
ChG	951	1.0	28.2	1.1
SiO_2	951	1.0	31.8	1.4
Si	950	1.1	31.6	0.7

2) UV Source

In the same manner as with the gamma ray case, the UV fluence and dose values were compared to an analytical calculation. Since the photon energy and the power density H of the UV source were known (E_p = 3.83 eV, H = 10 mW/cm^2), the source flux could be determined:

$$\phi = \frac{H}{E_p} = 1.63 \times 10^{16} \ \frac{\text{photons}}{\text{cm}^2 \cdot \text{s}}. \tag{23}$$

Multiplying Equation (23) by the area of the sample gives the photon emission rate. Using this value then allows the MCNP results to be reported as fluxes and dose rates instead of as fluences and doses normalized per source particle. The dose was converted from the default MeV/g to the more familiar radiation unit rad. The results were then multiplied by the ratio of the source area to the device area in order to account for the disk-like shape of the modeled source. The flux through the lateral device is shown in Figure 4.3.

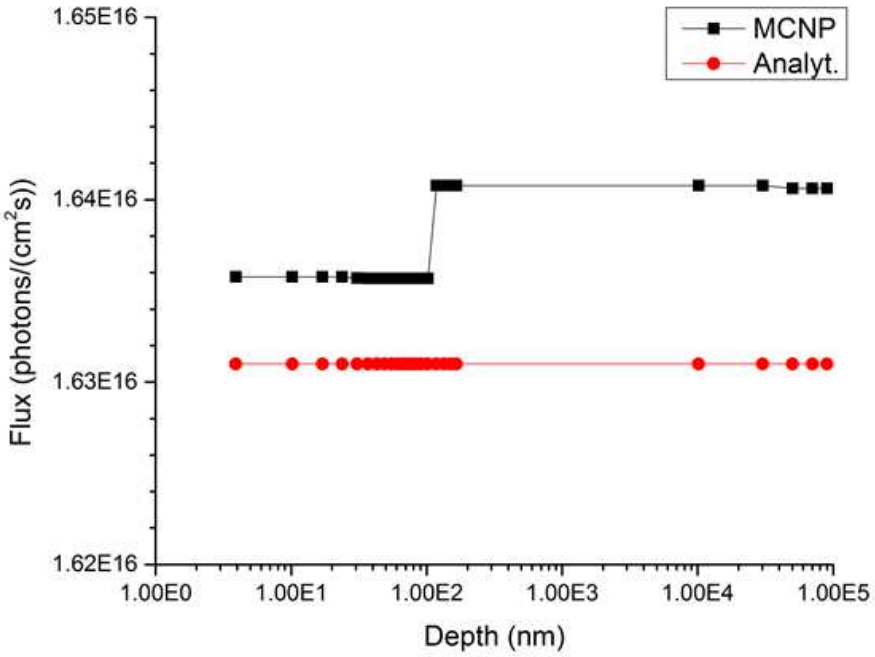

Figure 4.3. UV Flux in Lateral Device

As discussed in Chapter 3, Section C, the dose calculation which verifies the MCNP result may not represent reality too closely, but it demonstrates the basis of how MCNP results are determined in low-energy photon situations. The following uses Ag as an example. Using linear interpolation of EPDL data, the coherent scattering section for Ag at a photon energy of 3.827 eV was found to be σ_{CS} = 47.44 b. The number density for Ag was found to be 0.05847×10^{24} atoms/cm^3 and the density is 10.49 g/cm^3. Using Equation (2), the mass attenuation coefficient was determined to be 0.265 cm^2/g. Finally, using Equation (3), the UV photon dose normalized per source photon in Ag was found to be 9.75×10^{-4} MeV/g, which is close to the value obtained in MCNP of 9.64×10^{-4} MeV/g. When the incoherent scattering cross section of Ag $\sigma_{IS} = 1.65\times10^{-5}$ b is used in the calculation of the mass interaction coefficient, $\mu_{IS}/\rho = 9.20\times10^{-8}$ cm^2/g and the dose

was found to be 3.39×10^{-10} MeV/g. This value does not agree with MCNP results which demonstrates that the CS interaction is more important in determining the simulated UV doses.

In a similar manner, the rest of the dose rates for each material were calculated using the coherent scattering cross section and μ/ρ in place of μ_{en}/ρ in Equation (3). Figure 4.4 shows the results of the MCNP calculations and how they compare to the analytical values. The percent errors for the fluxes and dose rates are shown in Table 4.3. Although only three significant figures are shown for the flux, more decimal places were taken into consideration in the percent error calculation. It is interesting to note that the same dose rate results are produced whether the simulations are performed in MCNP5 or in MCNP6.1 even when the relevant .12p photon transport tables and lowering the photon energy cutoff to 1 eV were selected. This is because important photon interaction physics at low energies are not yet included in MCNP6.1 for most elements [25].

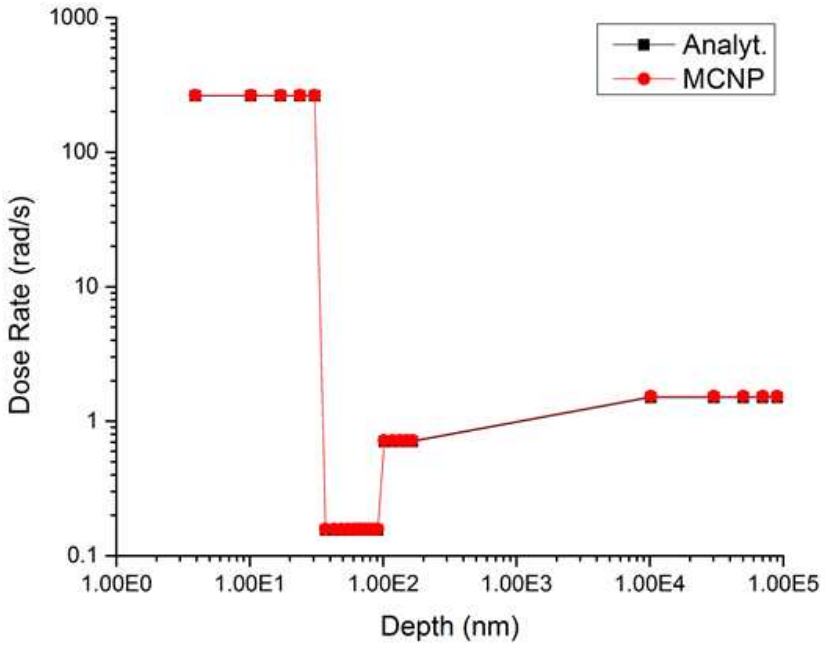

Figure 4.4. UV Dose Rate in Lateral Device

Table 4.3. Comparison of Analytical and Simulated UV Fluxes and Dose Rates

Material	Flux from MCNP [photons/(cm^2·s)]	Percent Error (%)	Dose Rate from MCNP (rad/s)	Percent Error (%)
Ag	1.64×10^{-16}	0.3	265	1.0
ChG	1.64×10^{-16}	0.3	0.158	1.6
SiO_2	1.64×10^{-16}	0.6	0.720	1.8
Si	1.64×10^{-16}	0.6	1.50	2.0

3) Electron Sources

The electron fluences and doses were determined using Equation (4) and Equation (11), respectively. The 100 keV electron results are shown in Figure 4.5 and Figure 4.6 while the 30 keV electron results are shown in Figure 4.7 and Figure 4.8.

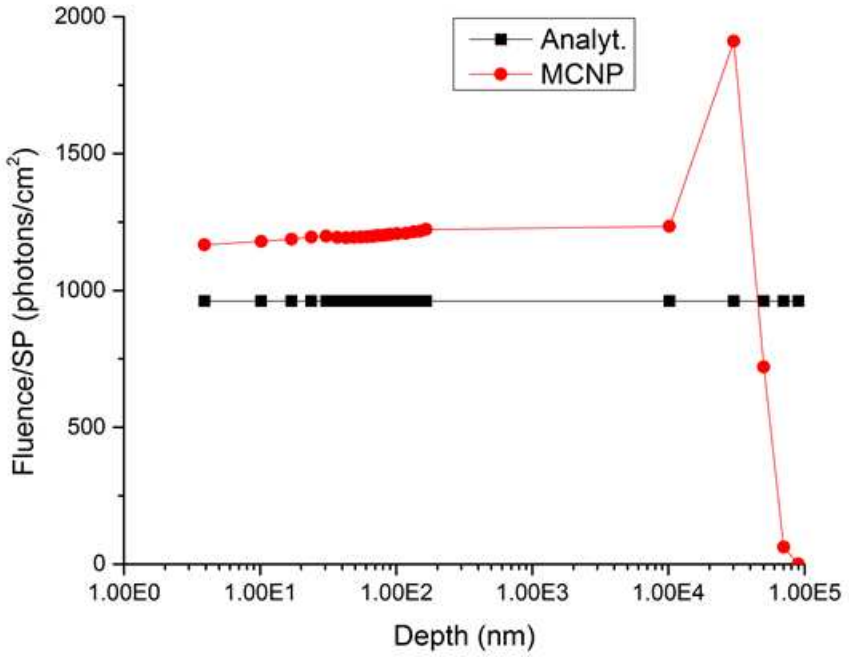

Figure 4.5. 100 keV Electron Fluence per Source Particle in Lateral Device

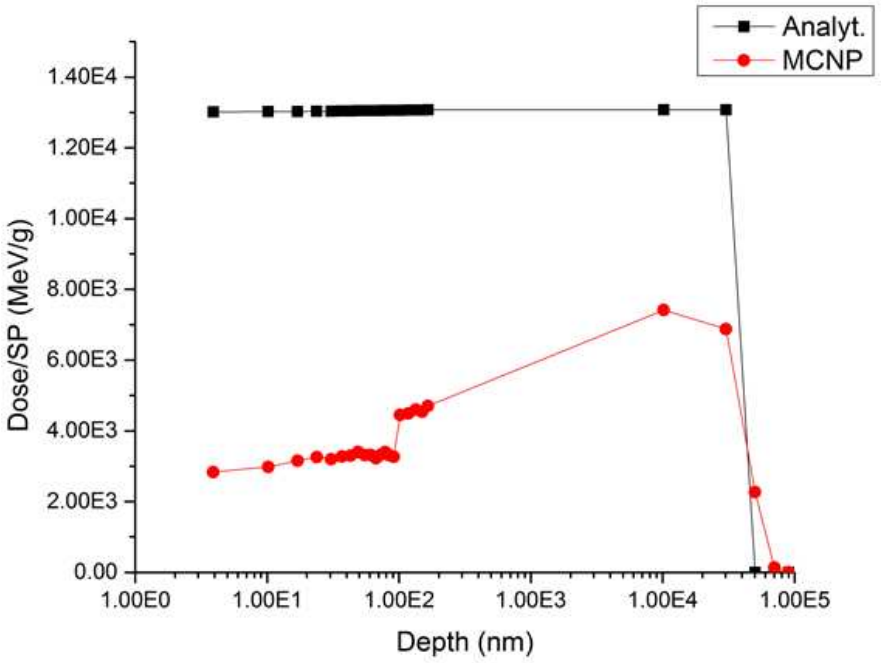

Figure 4.6. 100 keV Electron Dose per Source Particle in Lateral Device

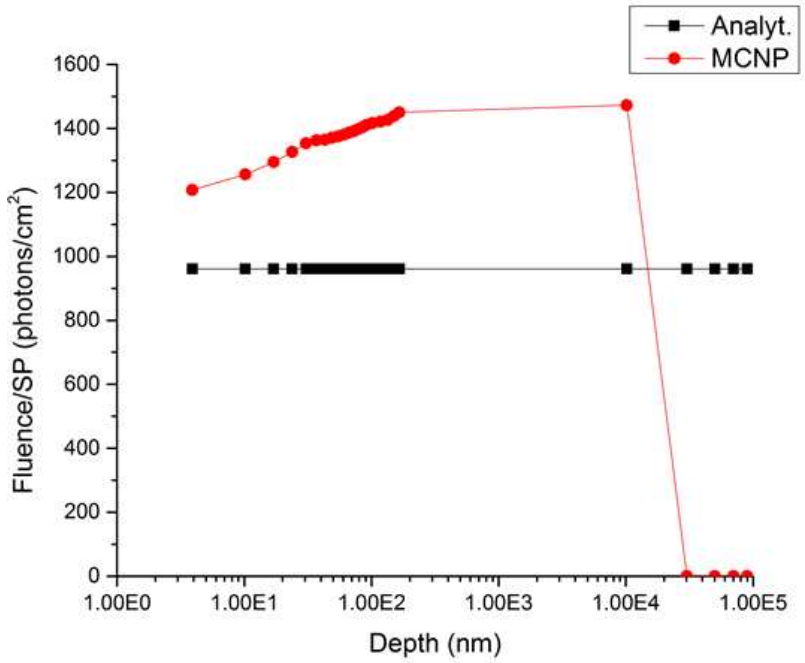

Figure 4.7. 30 keV Electron Fluence per Source Particle in Lateral Device

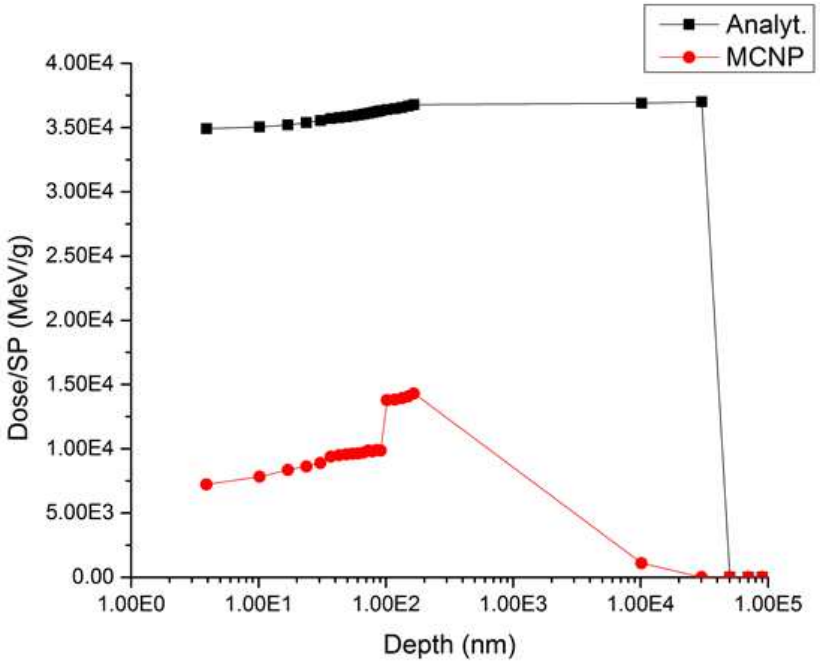

Figure 4.8. 30 keV Electron Dose per Source Particle in Lateral Device

In both of the electron source cases, the initial fluence at the surface of the Ag, which is plotted as the lowest depth value, was higher than the analytical calculation. This is because electrons have a preferential forward scattering, meaning electrons collide with other electrons as they move forward. MCNP also accounts for backscattering, which would increase the fluence across a surface even more. In the relatively thick Si material, which is plotted toward the higher depth values, the fluence drops to negligible values because neither the 100 keV nor the 30 keV electrons can reach that far into the material. For the thinner Ag, ChG, and SiO_2 layers, the penetration depth t_d is several orders of magnitude higher than the actual thickness t which means that electrons travel through them without losing a significant amount of energy. This is not the case for the Si layer, where t_d was determined to be less than 6 μm. Electrons deposit all of their energy well within the first 100 μm cell layer which is why the analytical dose drops to zero from the second Si cell onward.

The Katz-Penfold relation predicts a dose that is a factor of 1.8 to 4.6 times above the MCNP result for the 100 keV source and a factor of 2.6 to 4.8 times above that of the 30 keV source. Comparing the magnitudes of the electron dose cases reveals that the lower-energy 30 keV electrons result in a higher dose. This agrees with the Katz-Penfold relation, which shows that electrons with a lower energy have a lower maximum range, which means that the dose will increase due to the inverse relationship. This makes sense physically as well, as slower electrons will impart all of their energy in a thin layer instead of distributing that energy across a higher thickness. However, because the Katz-Penfold relation is material-independent, there is a strong disagreement between the

analytical and simulated values, especially as a function of depth. This suggests that on its own, the Katz-Penfold relation only weakly describes electron behavior.

Another method of determining the electron range uses the continuous-slowing-down approximation (CSDA), which describes the electron energy loss per unit length traveled due to Coulomb, atomic, and electron collisions [26]. The ESTAR program [27] calculates the CSDA range of electrons as a function of energy for user-defined materials. Using Ag as an example, the CSDA range at 100 keV is 0.02509 g/cm^2. The analytical electron dose becomes 7.00×10^3 MeV/g which is a factor of 2.5 above the MCNP result. For 30 keV electrons, the dose using the CSDA range in Ag is 1.56×10^4 MeV/g or 2.2 times higher than the MCNP result. These results are comparable to those obtained using Equation (7) for the maximum electron range. There does not appear to be any significant advantages to using the continuous-slowing-down approximation over the Katz-Penfold relation.

B. Vertical Device

1) Cobalt-60 Source

As with the lateral devices, the analytical fluence for each kind of source is the same since the same source geometry was used in each case. Contrary to the lateral devices, however, the vertical devices were photodoped with Ag. Therefore, the fluence and dose plots for each source include additional curves which highlight the effect of photodoping. The vertical devices have a different cross sectional area than the lateral devices, so a smaller source was simulated in MCNP. This smaller area leads to a photon fluence of

$$\Phi = \frac{S}{A} = \frac{1 \text{ photon}}{(2.50\times10^{-6} \text{ m})^2}\left(\frac{1 \text{ m}}{100 \text{ cm}}\right)^2 = 1.60\times10^{7} \text{ photons/cm}^2 . \quad (24)$$

Once again, all values are normalized per source particle.

The photon fluence as determined by MCNP is shown in Figure 4.9 with the analytical fluence plotted for different concentrations of Ag photodoping. All five curves overlap, showing a strong agreement between the analytical fluence and the MCNP results. Photodoping does not have a significant effect on the photon fluence.

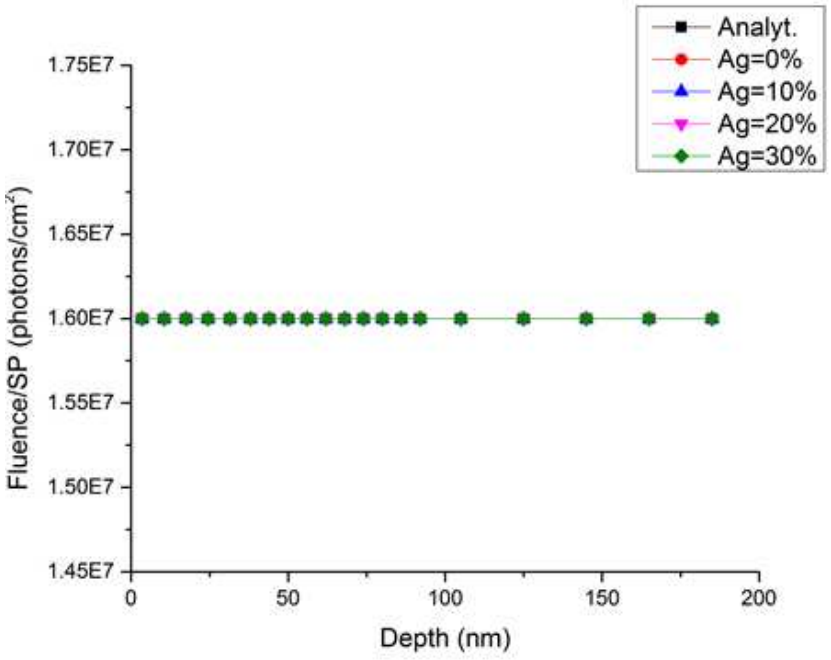

Figure 4.9. Co-60 Gamma Ray Fluence per Source Particle in Vertical Device

Using the same method as with the lateral devices, Table 4.4 summarizes the values of the mass-energy absorption coefficients for each material along with the analytical determination of the gamma doses. To three significant figures, μ_{en}/ρ for the ChG increases slightly with photodoping, and the effect can be seen in the result of the

gamma dose calculation. Figure 4.10 shows the gamma dose through the vertical device normalized per source particle obtained from MCNP. Table 4.5 shows the results from MCNP along with the percent difference between the simulated and analytical values. The MCNP results are shown to be slightly higher than the analytical calculations, but the percent difference is small.

Table 4.4. Analytical Co-60 Dose per Source Photon for the Vertical Device

Material	μ_{en}/ρ (cm^2/g)	D (MeV/g)
Ag	2.43×10^{-2}	4.86×10^{5}
ChG, Ag=0%	2.32×10^{-2}	4.64×10^{5}
ChG, Ag=10%	2.33×10^{-2}	4.67×10^{5}
ChG, Ag=20%	2.35×10^{-2}	4.69×10^{5}
ChG, Ag=30%	2.36×10^{-2}	4.72×10^{5}
Ni	2.54×10^{-2}	5.07×10^{5}

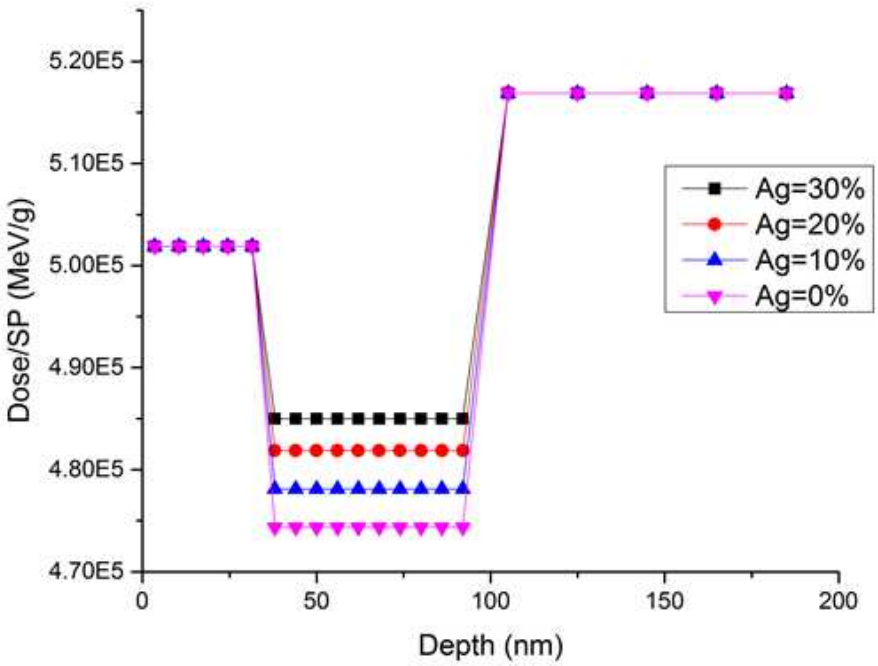

Figure 4.10. Co-60 Gamma Ray Dose per Source Particle in Vertical Device

Table 4.5. MCNP Dose per Source Gamma Ray and Percent Error for Comparison

Material	*D* (MeV/g)	Percent Error (%)
Ag	5.02×10^{5}	3.3
ChG, Ag=0%	4.74×10^{5}	2.2
ChG, Ag=10%	4.78×10^{5}	2.4
ChG, Ag=20%	4.82×10^{5}	2.8
ChG, Ag=30%	4.85×10^{5}	2.8
Ni	5.17×10^{5}	2.0

2) UV Source

As with the lateral devices, fluence and dose results were multiplied by the product of the source flux and the device area to obtain fluxes and dose rates. Figure 4.11 shows the UV flux plot against depth for various photodoping concentrations, and the analytical calculation agrees well with the simulated values. There was a slight variation in the flux observed in the deeper layers of the vertical structure, which is attributed to statistical error. Photodoping does not have a significant effect on photon flux.

A comparison between Figure 4.3 for the lateral device flux and Figure 4.11 for the vertical device flux shows that the fluxes are essentially equal when the number of source particles is taken into account. This may seem contrary to the other source cases, where the smaller vertical device appears to have a much higher fluence than the lateral device. The number of source particles takes the area of the device into account, which removes the effect of the per-source-particle normalization. Multiplying the fluxes shown in Figure 4.3 and Figure 4.11 by the area of the corresponding device shows that the total number of photons incident per second on the lateral device is higher, which is the intuitive result.

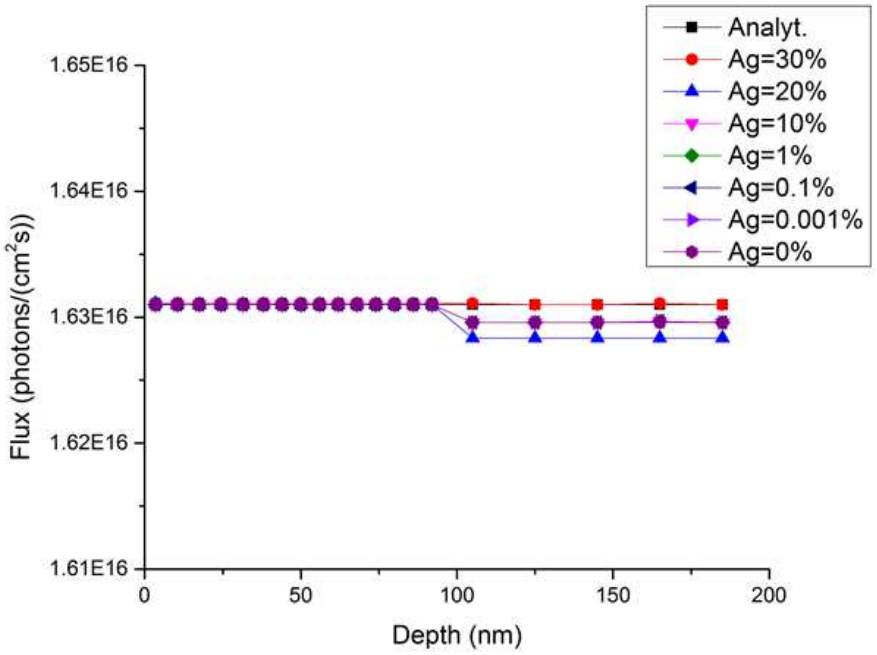

Figure 4.11. UV Flux in Vertical Device

In the same manner as with the lateral device UV case, the analytical UV dose rates for the vertical device were calculated and are shown in Table 4.6 along with the MCNP results. Figure 4.12 shows the UV dose rates obtained in MCNP. Note once again that the value utilized in this calculation is μ/ρ, not μ_{en}/ρ.

Table 4.6. UV Dose Rates in Each Material for Vertical Device

Material	μ/ρ (cm^2/g)	Analytical Dose Rate (rad/s)	MCNP Dose Rate (rad/s)	Percent Error (%)
Ag	2.65×10^{-1}	266	261	1.9
ChG, Ag=0%	1.67×10^{-4}	0.167	0.155	7.2
ChG, Ag=0.001%	1.71×10^{-4}	0.171	0.159	7.0
ChG, Ag=0.1%	5.38×10^{-4}	0.539	0.520	2.6
ChG, Ag=1%	3.88×10^{-3}	3.89	3.79	1.9
ChG, Ag=10%	3.59×10^{-2}	36.0	35.3	1.8
ChG, Ag=20%	6.90×10^{-2}	69.2	67.8	2.0
ChG, Ag=30%	9.97×10^{-2}	99.9	98.0	1.9
Ni	2.70×10^{-1}	271	268	1.1

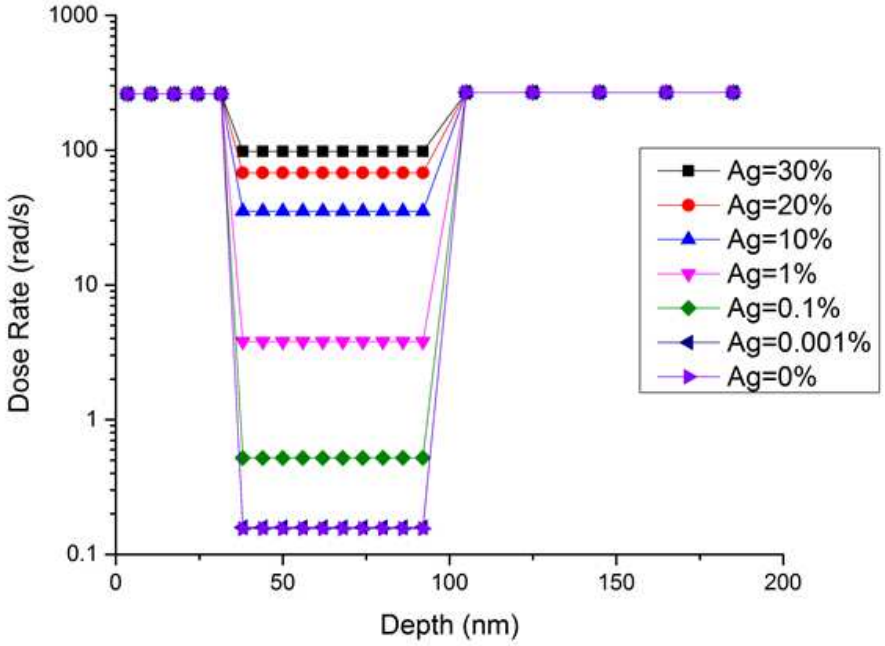

Figure 4.12. UV Dose Rate in Vertical Device

The dose rate in the ChG layer is shown to have an exponential dependence on photodoping. This is due to the much higher mass attenuation coefficient that Ag has compared to either Ge or Se. In each material, the UV dose rate is not observed to change as a function of depth. The percent errors for the UV dose rate cases are generally low,

which shows that the analytical calculation can be used to reliably predict an MCNP output despite the fact that the equation does not reflect how energy is deposited to a material in the physical situation.

3) Electron Sources

Figure 4.13 shows the 100 keV electron fluence per source particle. These results resemble the lateral case, where a preferential forward scattering of electrons causes the fluence to be greater than the analytical equation would predict. The fluence increases through the structure until the back end is reached, where electrons are less likely to backscatter off of the air layer. Photodoping does not have a significant impact on the fluence.

Figure 4.14 shows the 100 keV electron dose normalized per source particle. As with the 100 keV electrons with the lateral device, the Katz-Penfold relation overestimates the electron dose by a factor of about 2.8 to 3.7. The ChG dose is not affected by the amount of Ag photodoping in the material. Although the Katz-Penfold relation is valid up to any beta particle energy, these results suggest that the model may need to be modified into smaller energy brackets in order to produce more accurate dose values.

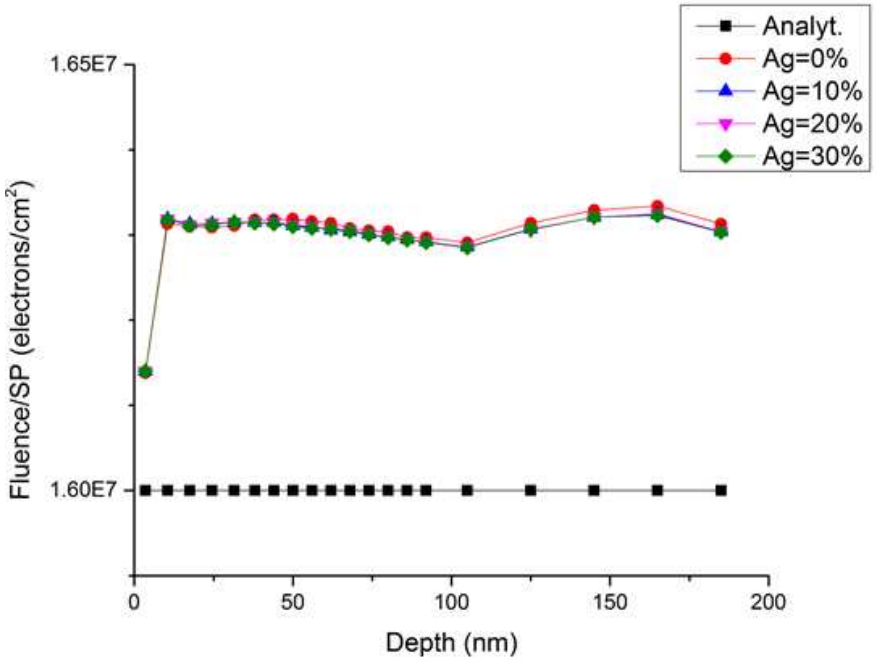

Figure 4.13. 100 keV Electron Fluence per Source Particle in Vertical Device

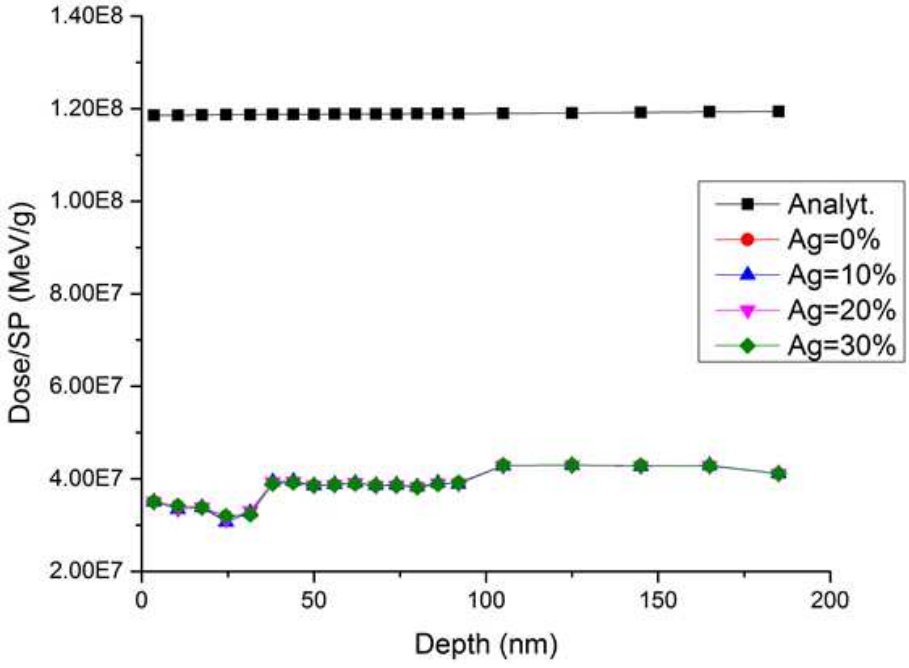

Figure 4.14. 100 keV Electron Dose per Source Particle in Vertical Device

Figure 4.15 and Figure 4.16 show the 30 keV electron fluence and dose, respectively, normalized per source particle. The analytical determination of the fluence is still low compared to the MCNP result, but the fluence is shown to experience a sudden drop after traversing the second Ag cell, which is contrary to the behavior shown by the lateral and vertical devices under the other electron source conditions. The vertical structure has a cross-sectional area that is much smaller than the lateral structure, and these low-energy electrons can collide more with the material, which could result in greater angular deflections that direct electrons out of the cell. The fluence is observed to increase in the thicker Ni layer. The Katz-Penfold relation over-predicts the 30 keV electron case by a factor of 2.6 to 3.6.

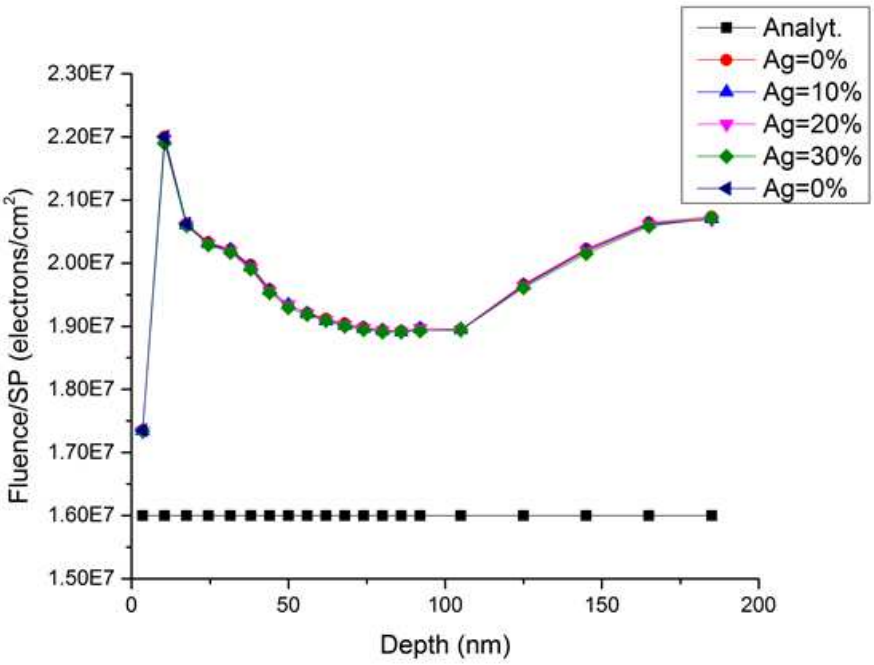

Figure 4.15. 30 keV Electron Fluence per Source Particle in Vertical Device

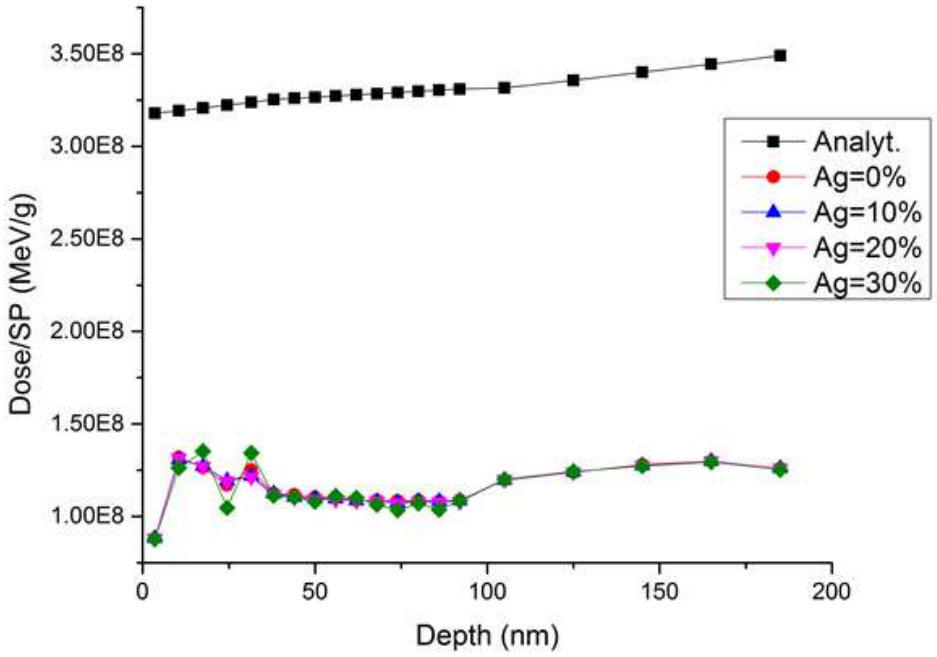

Figure 4.16. 30 keV Electron Dose per Source Particle in Vertical Device

5 NEUTRON HOWITZER

This chapter covers the design and source specifications of the neutron source. An analysis of gamma ray and neutron dose rates is also provided, along with a comparison between MCNP and experiment radioactivity measurements.

A. Design Overview

Designed by chemical engineering student Blake Anderson, Arizona State University's neutron source utilizes the spontaneous fission of Cf-252 to produce both neutrons and gamma rays which irradiate a sample. The californium in the source exists as Cf_2O_3. The source is made by suspending californium oxide particles in a palladium matrix which forms a cermet wire. The wire is then encased in a palladium tube, which is then encapsulated in a double layer of stainless steel. The composition of the californium is as follows: 2 w/o of Cf-249, 15 w/o of Cf-250, 4 w/o of Cf-251, and 79 w/o of Cf-252 [28].

The neutron howitzer had four major goals: 1) to use robust materials which provide support and longevity to the howitzer; 2) to increase the neutron flux through a sample via neutron moderation; 3) to effectively shield workers from neutron bombardment when the source is in the irradiation configuration; and 4) to grant ease of access to the irradiation chamber. Polyethylene, or $(C_2H_4)_n$, is used widely as a neutron moderator and was employed in this design in the regions directly surrounding the sample. Borated polyethylene was chosen as the neutron shielding material due to the high thermal neutron absorption cross-section of boron. Neutron fluence and dose characterization was not performed for the situation when the howitzer is in its storage configuration as it was assumed that the shipping container blocks most of the neutrons.

Figure 5.1 shows the assembled neutron howitzer. At the center of the howitzer is a half-cylinder shaped air chamber within which both the Cf-252 source and the sample will be situated. This chamber is attached to a rotating turntable which is made of polyethylene. Around the turntable is a wall of borated polyethylene to absorb neutrons before they scatter to the outside environment. A tube of borated polyethylene extends above the air chamber through which a steel cable connected to the source is threaded to the outside world. Below the air chamber is another borated polyethylene tube which provides more shielding while the howitzer is in its storage configuration.

Figure 5.1. Assembled Neutron Howitzer with Lead Shielding

MCNP simulations targeted two aspects of the howitzer. The first was to evaluate how well the polyethylene moderates neutrons by simulating the Cf-252 source in the

howitzer and comparing those measurements to a baseline calculation assuming it was done in a vacuum. Second, the effectiveness of the borated polyethylene layers to shield workers from neutron and gamma radiation was characterized by obtaining measurements at positions outside of the howitzer where human contact might be made.

B. Californium-252 Source Specifications

A source report from QSA Global provides a neutron emission rate of 2.3×10^{9} n/s per mg of Cf-252 [29]. The 25 μg of Cf-252 in ASU's source emits 5.75×10^{7} n/s. Again accounting for the mass of the Cf-252, the gamma dose rate of the source capsule in air at 1 m is 4.0 mR/hr or 0.974 μrad/s. The neutron dose rate in air is given to be 57.5 mrem/hr. Each spontaneous fission of Cf-252 releases an average of 3.7675 neutrons [30] and 10.3 photons [31]. Note that a Valentine report cites a value of 7.98 photons released per spontaneous fission [32]. The value stated in [32] provides the minimum bound for the number of photons released per spontaneous fission while [31] gives the upper bound. In this thesis, the value stated in [31] was chosen here to better match manufacturer data for the dose rates determined from MCNP simulations. Using these values, the gamma emission was found to be equal to 1.57×10^{8} γ/s.

The neutron spectrum was modeled in MCNP using the built-in Watt fission spectrum for Cf-252, which has the form [8]

$$f(E) = C\exp(-E/a)\sinh(\sqrt{bE}) \tag{25}$$

where C is a normalization constant, a = 1.025 MeV, b = 2.926 MeV^{-1}, and E is the energy of the neutron. When E is plotted from 0 MeV to 10 MeV, the spectrum shown in Figure 5.2 is obtained.

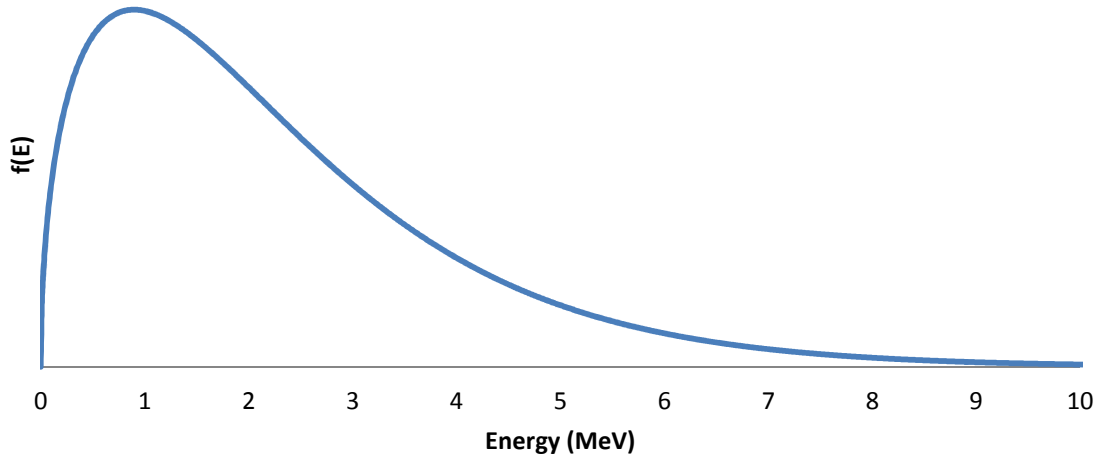

Figure 5.2. Watt Fission Spectrum for Cf-252

Significant research has been dedicated to characterizing the gamma ray spectrum of a Cf-252 source. It was not usually clear if the spectra accounted for more than the prompt gamma contributions, such as the amount of delayed gamma rays emitted from decay products and whether or not the detector efficiency was accounted for in the prompt spectrum. The detector efficiency is a ratio of the number of counts of radiation sensed at a particular energy to the total number of radiations emitted. Because this efficiency spectrum was normally not provided, any spectra that provided “counts” as a function of gamma ray energy [33-34] could not be reasonably compared to spectra that provided the actual number of gamma rays which already account for the efficiency. As such, two gamma ray spectra [35] which did provide the number of photons were simulated in MCNP and the results were compared to the manufacturer-given dose rates.

The first gamma spectrum simulated was provided by the manufacturer of ASU's Cf-252 source, QSA Global, which were calculated by Stoddard [36]. This spectrum is

used to calculate the dose rates stated on the product specification sheet. The second set of spectra account for both the gamma rays produced from the spontaneous fission of Cf-252 and the delayed gamma rays emitted from its decay products. The prompt gamma spectrum can be approximated by taking the prompt fission spectrum of U-235 and decreasing the limits by 0.1 MeV, shown in Equation (26), and the delayed gamma spectrum was approximated by Equation (27) [35].

$$N_{prompt}(E) = \begin{cases} 6.6 & 0 < E < 0.5 \text{ MeV} \\ 20.2e^{-1.78E} & 0.5 < E < 1.4 \text{ MeV} \\ 7.2e^{-1.09E} & 1.4 < E < 10.4 \text{ MeV} \end{cases} \tag{26}$$

$$N_{delayed}(E) = e^{-1.1E} \tag{27}$$

These were normalized and are shown in Figure 5.3. It is noticeable that the spectra do not have the same ranges, as shown by the abrupt stop in the “Manufacturer” curve at 6.5 MeV. Although the “Prompt” and “Delayed” curves include energies up to 10.4 MeV, their fraction of the overall spectrum is far smaller than those at lower energies. A separate simulation was performed to obtain the dose rate due to secondary gamma rays produced from (n,γ) reactions with the water phantom and the source capsule.

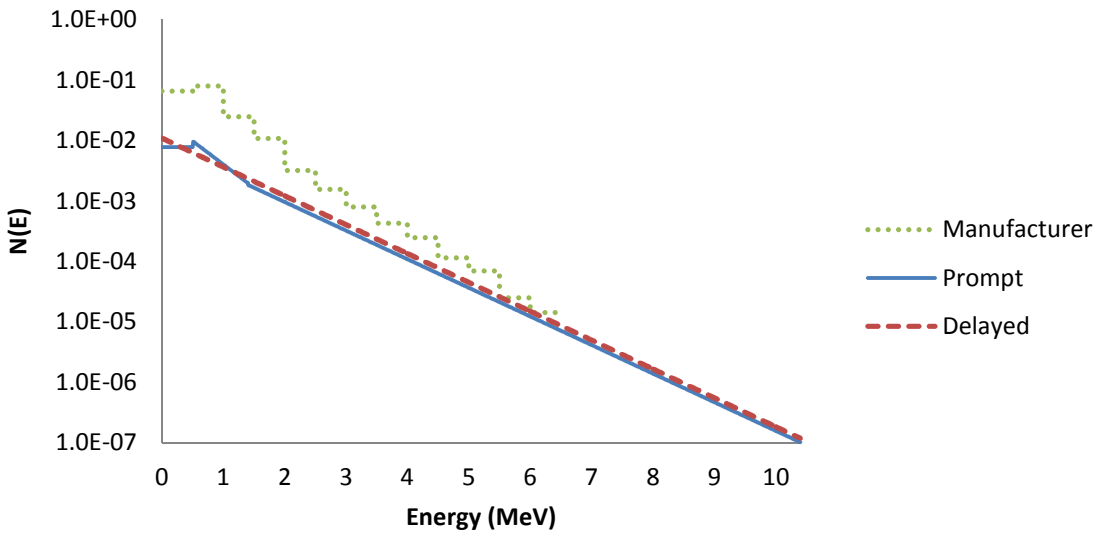

Figure 5.3. Normalized Gamma Spectra Modeled in MCNP

The Cf-252 source capsule was simulated in a sphere of dry air with a water phantom placed 1 m away. The four different gamma-ray sources were simulated in MCNP and the dose to the water phantom was obtained. The dose due to secondary gammas was added to the results of both the "QSA Global spectrum" and the "Prompt+delayed" results. Table 5.1 shows the results of the MCNP simulations. SP stands for “source particle”; for the secondary gammas, the source particle is a neutron, while the source particles for prompt and delayed gammas are photons. The dose rate column was determined by multiplying the Dose/SP by the appropriate source particle emission rate.

Table 5.1. Gamma Doses in Water Phantom from Cf-252 Source at 1 m

Description	Dose/SP (MeV/g)	Dose/SP (rad)	Dose Rate (μrad/s)
QSA Global value			0.974
QSA Global spectrum	1.57×10^{-7}	2.52×10^{-15}	0.395
Prompt gamma spectrum	1.67×10^{-7}	2.68×10^{-15}	0.421
Delayed gamma spectrum	1.75×10^{-7}	2.80×10^{-15}	0.439
Prompt+delayed	3.42×10^{-7}	5.48×10^{-15}	0.860
Secondary gammas	1.45×10^{-8}	2.32×10^{-16}	0.0134

The sum of the results from the QSA Global spectrum simulation and from the secondary gammas gives a total dose rate of 0.408 μrad/s, which is 41.9% of the stated value. Combining the prompt, delayed and secondary gamma results together gives a dose rate of 0.873 μrad/s, or 89.7% of the expected value. Clearly, when the delayed gammas are accounted for, the dose rate comes closer to the value quoted by the manufacturer. For this reason, the spectrum given by the manufacturer was not used in the modeling of the howitzer. Although the error of the combined effects of prompt and delayed gammas was somewhat large (10.3%), there were approximations made in producing those spectra. Hayes [35] noted that the 0.1 MeV decrease in the limits was made to account for the difference in average gamma ray energy between U-235 and Cf-252. The delayed gamma spectrum was described as “very approximate,” and the average number of photons emitted per neutron emitted has a range from 2.1 to 2.7, which could account for 22% of the error. More accurate spectra from more recent literature [33-34] might reduce the error.

C. Howitzer Performance

MCNP simulations were performed to quantify the neutron howitzer performance. First, the Cf-252 source capsule was simulated in air with a water phantom positioned

relative to where a sample would be located in the howitzer, about 6.35 cm away from the source. Once that baseline value for the non-moderated source particle fluence was obtained, the howitzer model was built around the source capsule and phantom, and the simulations were repeated. These results are shown in Table 5.2. The analytical calculation uses Equation (4) to determine the fluence of an isotropic point source at a distance of 6.35 cm. For this calculation, $S = 1$ and A is the area of a sphere with a radius of 6.35 cm since the Cf-252 source is isotropic as opposed to the photon and electron sources which were modeled as monodirectional. The fluence values were then multiplied by the Cf-252 neutron emission rate to produce a flux.

Table 5.2. Results of Simulations Comparing Source in Air Results to Source in Howitzer

Description	Fluence [n/(cm^2·SP)]	Flux [n/(cm^2·s)]
Analytical calculation	1.97×10^{-3}	1.13×10^{5}
Source capsule in air	2.08×10^{-3}	1.19×10^{5}
Source capsule in howitzer	5.64×10^{-3}	3.24×10^{5}

The analytical calculation assumes a point source in vacuum. When the Cf-252 source capsule is included in the simulation, the flux increases by 5% with respect to the point source case due to the neutron interactions with the stainless steel and palladium. When the source capsule is placed inside of the howitzer, the polyethylene moderates the neutrons, which increases the neutron flux even more to 2.86 times the value of the base case. This simulation, therefore, validates the need of the neutron howitzer moderator for radiation experiments: effectively, irradiation times would be almost three times longer without it when the neutron dose is considered.

Verifying the need of the howitzer in terms of how well it shields workers from neutron radiation required a simulation analysis at points where close contact would be made. This required two more water phantoms placed at the top and front of the howitzer. The water spheres outside of the borated polyethylene layer were larger than the sphere inside the radiation chamber in order to encourage more interactions with source particles, as the borated polyethylene was expected to absorb a significant amount of neutrons. Figure 5.4 shows a cross section of the MCNP-implemented geometry from different perspectives, which were obtained from the MCNPX Visual Editor (Vised). The simulations were repeated to obtain the fluence and dose for both neutrons and gamma rays.

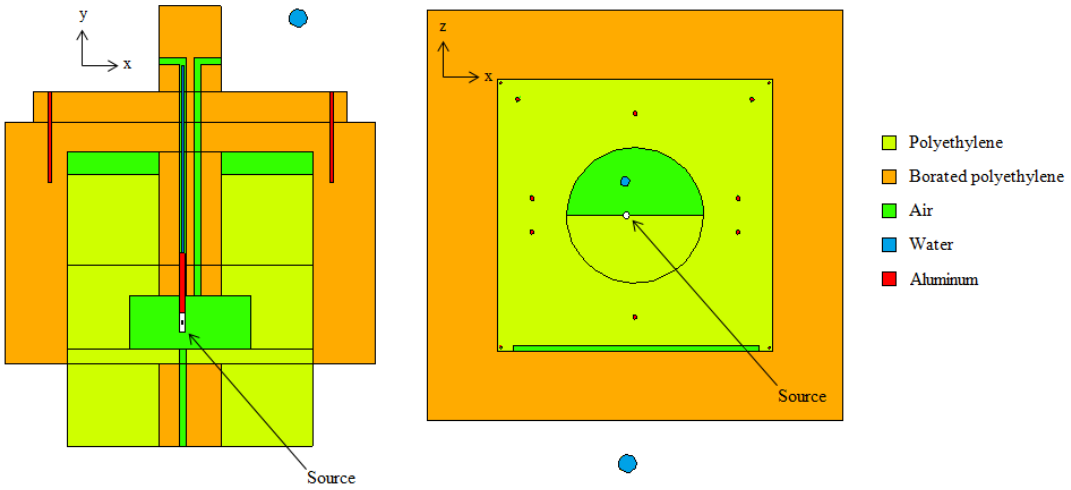

Figure 5.4. Neutron howitzer as Implemented in MCNP; Models from Vised

Table 5.3, Table 5.4, and Table 5.5 show the results of the MCNP simulations for gamma rays for the water phantom inside of the chamber and for those at the front and top of the howitzer. A total of three simulations were performed to analyze the effects of

the prompt and delayed gammas along with the secondary gammas and neutrons. As with the SP designations used in Table 5.1, the flux and dose rate columns were determined by multiplying the fluence/SP and dose/SP, respectively, by the appropriate source particle emission rate.

Table 5.3. Gamma Flux and Dose Rate Results of the Sphere inside the Chamber

	Fluence/SP (particles/cm^2)	Flux [particles/(cm^2·s)]	Dose/SP (MeV/g)	Dose/SP (rad)	Dose Rate (μrad/s)
Secondary Gammas	1.18×10^{-3}	6.77×10^{4}	2.97×10^{-5}	4.75×10^{-13}	27.3
Prompt Gammas	2.55×10^{-3}	1.47×10^{5}	4.51×10^{-5}	7.22×10^{-13}	113
Delayed Gammas	2.44×10^{-3}	1.40×10^{5}	4.65×10^{-5}	7.44×10^{-13}	117
Total Gammas	6.17×10^{-3}	3.55×10^{5}	1.21×10^{-4}	1.94×10^{-12}	258

Table 5.4. Gamma Flux and Dose Rate Results of the Sphere at the Front of the Source

	Fluence/SP (particles/cm^2)	Flux [particles/(cm^2·s)]	Dose/SP (MeV/g)	Dose/SP (rad)	Dose Rate (μrad/s)
Secondary Gammas	6.80×10^{-5}	3.91×10^{3}	1.44×10^{-6}	2.30×10^{-14}	1.32
Prompt Gammas	5.11×10^{-5}	2.93×10^{3}	5.92×10^{-7}	9.48×10^{-15}	1.49
Delayed Gammas	4.93×10^{-5}	2.84×10^{3}	6.38×10^{-7}	1.02×10^{-14}	1.60
Total Gammas	1.68×10^{-4}	9.68×10^{3}	2.67×10^{-6}	4.27×10^{-14}	4.41

Table 5.5. Gamma Flux and Dose Rate Results of the Sphere at the Top of the Source

	Fluence/SP (particles/cm^2)	Flux [particles/(cm^2·s)]	Dose/SP (MeV/g)	Dose/SP (rad)	Dose Rate (μrad/s)
Secondary Gammas	5.02×10^{-5}	2.88×10^{3}	8.55×10^{-7}	1.37×10^{-14}	0.79
Prompt Gammas	2.90×10^{-5}	1.67×10^{3}	2.81×10^{-7}	4.50×10^{-15}	0.71
Delayed Gammas	2.85×10^{-5}	1.64×10^{3}	2.97×10^{-7}	4.75×10^{-15}	0.75
Total Gammas	1.08×10^{-4}	6.19×10^{3}	1.43×10^{-6}	2.29×10^{-14}	2.24

Figure 5.5 demonstrates how the neutron howitzer affects the flight path of both neutrons and photons. Neutrons are generally kept within the polyethylene portions of the howitzer, but those that escape into the borated polyethylene layers are quickly absorbed, which is shown by the increasingly decaying amount of neutrons as they travel away from the center. Gamma rays are not attenuated significantly by the borated polyethylene, which explains why the gamma dose is several times higher at the side and top of the howitzer compared to the neutron dose.

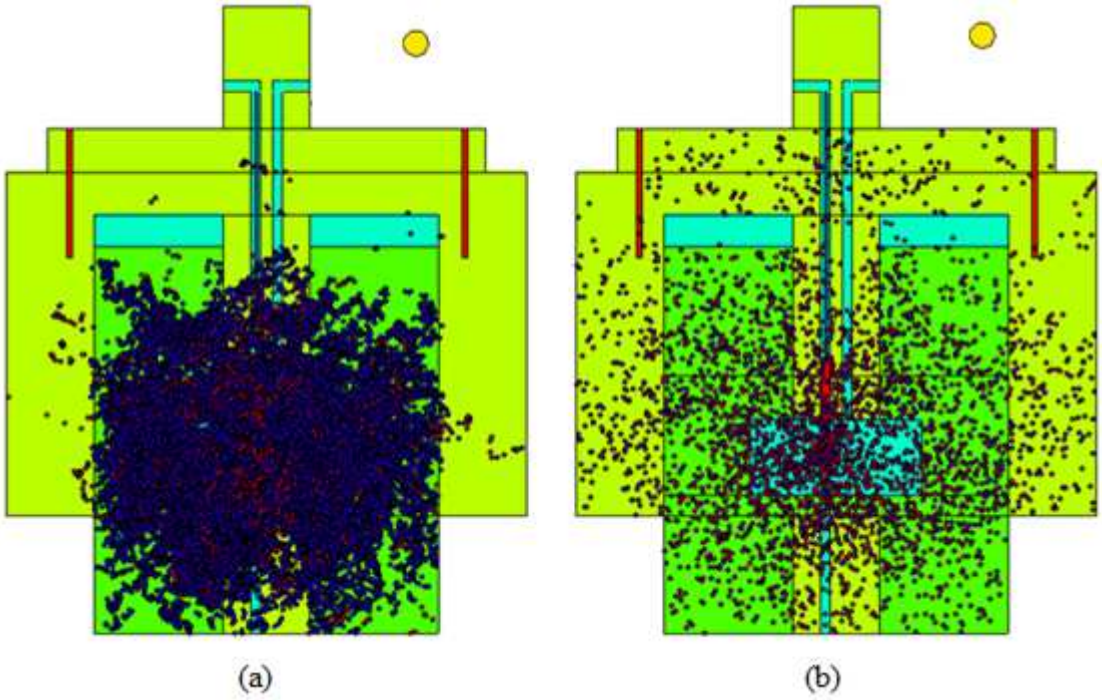

Figure 5.5. a) Neutron and b) Gamma Ray Interactions with the Howitzer

Physical measurements of the gamma and neutron dose rates were taken at locations outside of the howitzer corresponding to the locations of the water phantoms. The locations of the water phantoms simulated in MCNP correspond to the geometry of

the radiation counters used to obtain the measurement. In Figure 5.4 and Figure 5.5, the water phantoms were placed 4.5 inches away from the front and top of the howitzer to account for the diameter of the Ludlum 9-inch REM ball in the neutron dose measurements. The gamma dose measurements were taken much closer to the surface of the howitzer and the water phantoms in MCNP were placed accordingly.

The results for the gamma ray simulations are shown in Table 5.6. The simulated gamma dose rates taken from Table 5.4 for the front measurement and Table 5.5 for the top measurement are also shown in Table 5.6. The disagreements for the gamma dose rates are low. This demonstrates the effectiveness of the simulated neutron howitzer model in duplicating the gamma ray results of the actual howitzer.

Table 5.6. Comparison of Measured Howitzer Dose Rates to Simulated Values

Description	Dose Rate, Measured (μrad/s)	Dose Rate, Simulated (μrad/s)	Percent Error (%)
Gamma, front	4.39	4.41	0.5
Gamma, top	2.19	2.24	2.3

The percent errors are relatively small, which shows that the environment of the simulated neutron howitzer matches well with real-life. By extension, the Cf-252 source capsule model reasonably reflects the performance of the physical source when the gamma dose rate is considered. The error between the gamma dose rate provided by the manufacturer and the simulated values is comparatively high (10.3%). The gamma dose rate provided by the manufacturer uses data from a source that is quite dated (1965) and uses a low-resolution gamma spectrum with energy intervals of 0.5 MeV. More recent research [33-34] has characterized the gamma ray spectrum to much finer intervals,

although their spectra were not considered in this thesis due to their detector efficiency curves being unknown. All of these factors suggest that the manufacturer-quoted gamma dose rate may actually be too high.

Multiple neutron energy bins were tallied in MCNP to obtain the neutron dose per source neutron at the water phantom locations. These energy bins were chosen to be the halfway points between stated energy values from the tabulated list of neutron quality factors in [37]. The MCNP doses were then converted to units of rem by multiplying the dose in rad by the quality factor of the neutrons between certain energies, which were then multiplied by the neutron emission rate. The sum of the neutron doses in mrem/hr showed the final dose rate. These results are shown in Table 5.7, Table 5.8, and Table 5.9. A comparison of the neutron dose rate measurements and simulation results for the front and top of the howitzer is shown in Table 5.10.

Table 5.7. Neutron Dose Results of the Sphere inside the Chamber

Energy Range (MeV)	Quality Factor	Dose/SP (MeV/g)	Dose Rate (mrem/hr)
0 – 0.005	2	2.65×10^{-7}	1.75
0.005 – 0.05	2.5	2.44×10^{-6}	20.2
0.05 – 0.25	7.5	1.31×10^{-5}	3.27×10^{2}
0.25 – 1.25	11	1.05×10^{-4}	3.82×10^{3}
1.25 – 3.75	9	2.26×10^{-4}	6.72×10^{3}
3.75 – 6	8	7.05×10^{-5}	1.87×10^{3}
6 – 8.5	7	2.06×10^{-5}	4.79×10^{2}
8.5 – 12	6.5	4.74×10^{-6}	1.02×10^{2}
12 – 17	7.5	4.57×10^{-7}	11.4
17 – 30	8	1.10×10^{-8}	2.91×10^{-1}
Total		4.43×10^{-4}	1.34×10^{4}

Table 5.8. Neutron Dose Results of the Sphere at the Front of the Source

Energy Range (MeV)	Quality Factor	Dose/SP (MeV/g)	Dose Rate (mrem/hr)
0 – 0.005	2	6.30×10^{-11}	4.17×10^{-4}
0.005 – 0.05	2.5	6.57×10^{-10}	5.44×10^{-3}
0.05 – 0.25	7.5	3.62×10^{-9}	8.98×10^{-2}
0.25 – 1.25	11	2.03×10^{-8}	7.41×10^{-1}
1.25 – 3.75	9	5.34×10^{-8}	1.59
3.75 – 6	8	3.78×10^{-8}	1.00
6 – 8.5	7	1.90×10^{-8}	4.40×10^{-1}
8.5 – 12	6.5	6.85×10^{-9}	1.48×10^{-1}
12 – 17	7.5	0.00	0.00
17 – 30	8	0.00	0.00
Total		1.42×10^{-7}	4.02

Table 5.9. Neutron Dose Results of the Sphere at the Top of the Source

Energy Range (MeV)	Quality Factor	Dose/SP (MeV/g)	Dose Rate (mrem/hr)
0 – 0.005	2	2.38×10^{-11}	1.58×10^{-4}
0.005 – 0.05	2.5	2.70×10^{-10}	2.23×10^{-3}
0.05 – 0.25	7.5	1.34×10^{-9}	3.32×10^{-2}
0.25 – 1.25	11	7.54×10^{-9}	2.75×10^{-1}
1.25 – 3.75	9	2.09×10^{-8}	6.22×10^{-1}
3.75 – 6	8	1.67×10^{-8}	4.42×10^{-1}
6 – 8.5	7	9.31×10^{-9}	2.16×10^{-1}
8.5 – 12	6.5	3.12×10^{-9}	6.71×10^{-2}
12 – 17	7.5	0.00	0.00
17 – 30	8	0.00	0.00
Total		5.91×10^{-8}	1.66

Table 5.10. Comparison of Measured Neutron Dose Rates to Simulated Values

Description	Dose Rate, Measured (mrem/hr)	Dose Rate, Simulated (mrem/hr)	Percent Error (%)
Neutron, front	4.2	4.02	4.3
Neutron, top	2.2	1.66	24.5

It is not feasible to compare measured neutron dose values to simulated values for samples inside of the chamber since the REM ball cannot fit inside the chamber. Despite this fact, it is reasonable to assume that if the MCNP results and the measured values are "close enough," the dose rate obtained for samples inside the chamber would also be reasonably accurate. As shown in Table 5.10, for the front of the source, there is a 4.3% difference between the MCNP results and the measured value, while the top of the source has a much larger 24.5% difference. At first, this latter difference appears to be unacceptably large, but it could be explained by human error. An additional simulation was performed to analyze the impact of moving the Cf-252 source just 0.5 inches (1.27

cm) upward, which is well within the range defined by the piece of tape on the howitzer cable showing that the howitzer is in its irradiation mode. The dose rate at the front of the howitzer decreased to 3.87 mrem/hr for a percent difference of 7.9% while the dose rate at the top increased to 1.91 mrem/hr and a difference of 13.2%. The latter percent difference is still high, but moving the source a seemingly insignificant amount further upward would decrease the difference even more. Also, the readout on the Ludlum REM ball was not stable, so the stated dose rate could have been as low as 2.1 mrem/hr, which would bring the percent error for the top measurement down to 9.0%. The Ludlum REM ball user manual [38] states that the "reading [is] within 10% of true value with detector connected." Because the simulated and measured values are within or close to this 10% margin, the MCNP model developed is determined to be effective in modeling the neutron howitzer. It can therefore be concluded that the dose rate determined for samples within the chamber is also reasonably accurate.

Materials that undergo neutron irradiation become radioactive, and the neutron-induced gamma ray activity is characteristic of a particular element. This neutron activation effect was analyzed using radiation foils of various elements and a Canberra gamma ray spectroscopy system. The activity of the radioactive progeny of an isotope irradiated can be determined by [39]

$$A(t) = \frac{\gamma_i N_A m_{elem}}{M_{elem}} \left(\frac{\sqrt{\pi}}{2} \sigma_{th} \phi_{th} + RI \phi_{epi} \right) \left(1 - e^{-\frac{(\ln 2)t}{t_{1/2}}} \right) \tag{28}$$

where γ_i is the isotopic abundance of the particular nuclide, N_A is Avogadro's number, m_{elem} is the mass of the sample, M_{elem} is the atomic weight of the element, σ_{th} is the thermal neutron absorption cross section, ϕ_{th} is the thermal flux of neutrons up to 0.5 eV,

RI is the resonance integral for epithermal neutrons, ϕ_{epi} is the epithermal flux of neutrons having energies between 0.5 eV and 1 keV, *t* is the irradiation time, and $t_{1/2}$ is the half-life of the radioactive progeny of the target isotope.

In order to bring the radiation foils relatively close to their respective saturation points, the exponential term at the right-hand side of Equation (28), denoted *Z*, was set to 0.9961 and solved for *t*. The value of 0.9961 corresponds to the fraction of radioactive atoms that would have decayed after eight half-lives elapse, or $t/t_{1/2} = 8$. The half-lives considered here were of the shorter-lived isotopes in an element, e.g., Ni-65 instead of Ni-59 or Ni-63 because it is not practical to irradiate those longer-lived isotopes to saturation. The actual irradiation time was chosen to be some value that is near to or greater than the time determined by the previous calculation. The one exception was scandium which could not be brought to saturation due to its relatively long half-life (83.8 days). Regardless, an irradiation time of approximately one month was chosen for the scandium foil to see how much information can be obtained.

In total, five foils were irradiated and analyzed: scandium, nickel, copper, zirconium, and gold. Other foils composed of aluminum, vanadium, and indium were also irradiated, but their results were not considered here because their spectroscopy results were deemed unreliable. Because Al and V have relatively short half-lives these foils decayed significantly during the transfer from the howitzer to the spectroscopy system located in a different building, resulting in a large error. The In results were rejected because isotopes could not be identified correctly by the spectroscopy system. The foils had a high purity of at least 99.74%, so m_{elem} and M_{elem} in Equation (28) were approximated to be the masses and atomic weights of the foils themselves. The values for

the thermal neutron absorption cross section and the resonance integral were found on a chart of the nuclides [40]. MCNP was used to obtain the fluences per source neutron within the thermal and epithermal ranges in the water phantom located inside of the radiation chamber. Multiplying the results from MCNP by the neutron emission rate gives:

$$\begin{aligned} \phi_{th} &= 1.30 \times 10^{5} \text{ neutrons/(cm}^2\text{s)} \\ \phi_{epi} &= 3.21 \times 10^{4} \text{ neutrons/(cm}^2\text{s)} \end{aligned} . \quad (29)$$

These flux values are assumed to remain constant for each foil since they are thin, which encourages neutrons to pass straight through them instead of backscattering.

The data and the results of the analytical calculation using Equation (28) for each radioactive product are shown in Table 5.11 and extend into Table 5.12. The foil volume is also included in Table 5.11 for convenience. Only those nuclides with radioactive progeny due to radiative capture (n,γ) were analyzed in this work. The spectroscopy system also accounts for gamma rays emitted due to other types of reactions, but those contributions were comparatively small and noisy and were thus ignored in the analysis.

Table 5.11. Data of Activation Foils Used in Equation (28)

Target Nuclide	Isotopic Abundance	Radio-active Progeny	Foil Mass (g)	Foil Volume (cm^3)	Thermal Absorption Cross-Section (b)	Resonance Integral (b)
Sc-45	1	Sc-46	0.0516	1.61×10^{-2}	17	7
Ni-58	0.681	Ni-59	0.2826	3.22×10^{-2}	4.6	2.2
Ni-62	0.011	Ni-63	0.2826	3.22×10^{-2}	14.5	6.6
Ni-64	0.0093	Ni-65	0.2826	3.22×10^{-2}	1.6	1.2
Cu-63	0.6917	Cu-64	0.143	1.61×10^{-2}	4.5	5
Cu-65	0.3083	Cu-65	0.143	1.61×10^{-2}	2.17	2.2
Zr-92	0.1715	Zr-93	0.112	1.61×10^{-2}	0.2	0.6
Zr-94	0.1738	Zr-95	0.112	1.61×10^{-2}	0.05	0.28
Zr-96	0.028	Zr-97	0.112	1.61×10^{-2}	0.022	5.1
Au-197	1	Au-198	0.124	6.44×10^{-3}	98.7	1550

Table 5.12. Radioactivity of Activation Foils According to Equation (28)

Radioactive Progeny	Half-Life (s)	Time Needed for Z = 0.9961 (s)	Irradiation Time (s)	Radioactivity of progeny (μCi)
Sc-46	7.24×10^{6}	5.79×10^{7}	3 008 700	1.02×10^{-2}
Ni-59	2.40×10^{12}	1.92×10^{13}	76 380	7.10×10^{-10}
Ni-63	3.19×10^{9}	2.55×10^{10}	76 380	2.80×10^{-8}
Ni-65	9.06×10^{3}	7.25×10^{4}	76 380	1.62×10^{-4}
Cu-64	4.57×10^{4}	3.66×10^{5}	501 720	1.72×10^{-2}
Cu-66	3.06×10^{2}	2.45×10^{3}	501 720	3.63×10^{-3}
Zr-93	4.73×10^{13}	3.78×10^{14}	434 340	9.24×10^{-13}
Zr-95	5.53×10^{6}	4.43×10^{7}	434 340	2.72×10^{-6}
Zr-97	6.03×10^{4}	4.82×10^{5}	434 340	9.23×10^{-5}
Au-198	2.33×10^{5}	1.86×10^{6}	1 731 900	0.623

The foils were modeled in MCNP to obtain a simulated estimate of the activity. One of the many iterations of code used to produce the data in this section is given in the Appendix. Each foil replaced the water phantom inside of the irradiation chamber of the model. The holding apparatus for each foil was also modeled, which consisted of a vinyl tube that contained the foil and a vinyl mount. A diagram of the foil and the holder is

shown in Figure 5.6. The number of (n,γ) reactions that occur per source particle is obtained in MCNP by multiplying the output from an F4-type tally by the number density of a particular isotope, the radiative capture cross section, and the volume of the foil. As an equation, the number of reactions of the *k-th* type is

$$R_k = \Phi N \sigma_k V \tag{30}$$

where N is the number density for a particular isotope, σ_k is the cross section of the *k-th* type, and V is the volume. Using substitutions, Equation (30) can also be rewritten as

$$R_k = \sigma_k n_1 \Phi \tag{31}$$

where n_1 is the number of target atoms. The simulation results in units of [number of (n,γ) reactions/SP] for each isotope are summarized in Table 5.13.

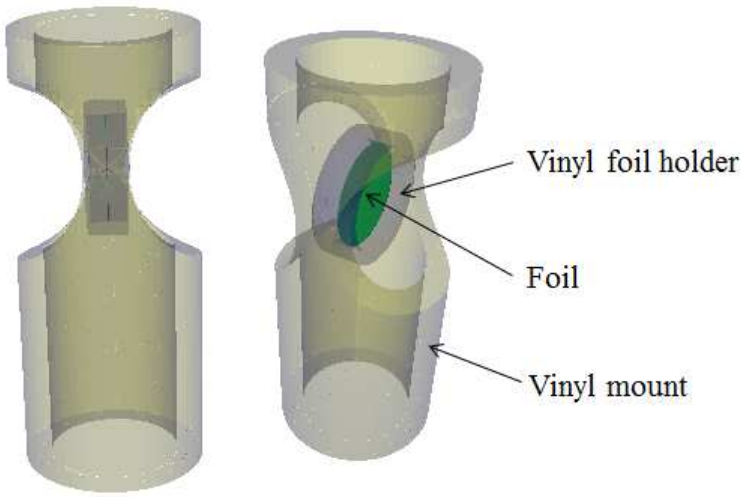

Figure 5.6. Model of the Activation Foil and the Holding Apparatus

Table 5.13. MCNP Results for the Activation Foils in the Neutron Howitzer

Radioactive Progeny	MCNP Reactions (number of reactions/SP)
Sc-46	2.90×10^{-5}
Ni-59	1.37×10^{-5}
Ni-63	7.31×10^{-7}
Ni-65	1.86×10^{-7}
Cu-64	6.23×10^{-6}
Cu-66	2.78×10^{-6}
Zr-93	4.95×10^{-8}
Zr-95	5.01×10^{-8}
Zr-97	8.07×10^{-9}
Au-198	7.14×10^{-5}

In order to interpret these MCNP results in a meaningful way, the theory of nuclear transmutation [41] must be briefly discussed. For an initial amount of target atoms $n_1(0)$, the number of activated atoms $n_2(t)$ at time t during an irradiation session is equal to

$$n_2(t) = \frac{\sigma_{a,1} n_1(0) \phi}{\lambda_2} \left(1 - e^{-\lambda_2 t}\right) \tag{32}$$

where $\sigma_{a,1}$ is the microscopic capture cross section of the target nuclide, ϕ is the neutron flux, and λ_2 is the decay constant of the activation product. Using this value, the activity of the radioactive product is defined to be

$$A_2(t) \equiv \lambda_2 n_2(t) = \sigma_{a,1} n_1(0) \phi \left(1 - e^{-\lambda_2 t}\right). \tag{33}$$

As $t \to \infty$, Equation (33) can be simplified to

$$A_2(t \to \infty) = \sigma_{a,1} n_1(0) \phi \,. \tag{34}$$

Although Equation (31) cannot be directly compared to Equation (34), because the fluence from MCNP is given per source particle, multiplying Equation (31) by the neutron source emission rate n_{sp} gives the reaction rate in terms of flux:

$$RR_k = \sigma_k n_1 \Phi n_{sp} = \sigma_k n_1 \phi . \tag{35}$$

The relevant reaction in this case is radiative capture, so the cross section in Equation (35) is equal to that of Equation (34). Therefore, MCNP can be used to find the maximum theoretical activity of a radioactive product simply by multiplying the MCNP results by the neutron emission rate. These findings are shown in Table 5.14 after converting from the default activity unit in Bq to μCi.

Table 5.14. Activity Derived from MCNP Results

Radioactive Progeny	MCNP Activity (μCi)
Sc-46	4.51×10^{-2}
Ni-59	2.13×10^{-2}
Ni-63	1.14×10^{-3}
Ni-65	2.89×10^{-4}
Cu-64	9.68×10^{-3}
Cu-66	4.32×10^{-3}
Zr-93	7.69×10^{-5}
Zr-95	7.79×10^{-5}
Zr-97	1.26×10^{-5}
Au-198	0.111

An experimental value for the activity was obtained by placing each foil in the radiation chamber at the same distance as in the MCNP model. Each foil was irradiated for the amount of time stated in Table 5.12. There was a cooling time t_c during which the foil was transported from the neutron howitzer to the spectroscopy system in another

building. The measured activity A_{meas} was converted to an induced activity A_{ind} by the following relationship, which determines the activity at the moment the foil was retrieved from the howitzer, i.e., as if the cooling time was zero:

$$A_{ind} = A_{meas} e^{\lambda_2 t_c} . \tag{36}$$

The induced activity for the Sc-46 product had to be modified since that particular foil was not brought to saturation. When a radiation foil is brought to saturation, the value of A_{ind} in Equation (36) represents the maximum activity $A_{\max}$. The activity as a function of irradiation time is

$$A(t) = A_{\max} \left(1 - e^{-\lambda_2 t}\right) . \tag{37}$$

At saturation, Equation (36) can be reinterpreted as

$$A_{ind} = A_{\max} = \frac{A(t)}{1 - e^{-\lambda_2 t}} = \frac{A_{meas} e^{\lambda_2 t_c}}{1 - e^{-\lambda_2 t}} . \tag{38}$$

Equation (38) generalizes Equation (36) for any amount of irradiation time *t*.

The values of the activities obtained in all three ways are summarized in Table 5.15. Some of the entries for the induced activity were left blank as they were not identified by the spectroscopy system.

Table 5.15. Activities Obtained via Calculation, Simulation, and Experimentation

Radio-active Progeny	Simulated Activity (μCi)	Analytical Activity (μCi)	Simulated-to-Analytical Ratio	Induced Activity (μCi)	Simulated-to-Induced ratio
Sc-46	4.51×10^{-2}	1.02×10^{-2}	4.4	3.01×10^{-2}	1.5
Ni-59	2.13×10^{-2}	7.10×10^{-10}	3.0×10^{7}		
Ni-63	1.14×10^{-3}	2.80×10^{-8}	4.0×10^{4}		
Ni-65	2.89×10^{-4}	1.62×10^{-4}	1.8	1.95×10^{-4}	1.5
Cu-64	9.68×10^{-3}	1.72×10^{-2}	0.56	0.0128	0.76
Cu-66	4.32×10^{-3}	3.63×10^{-3}	1.2		
Zr-93	7.69×10^{-5}	9.24×10^{-13}	8.3×10^{7}		
Zr-95	7.79×10^{-5}	2.72×10^{-6}	29		
Zr-97	1.26×10^{-5}	9.23×10^{-5}	0.14	8.73×10^{-6}	1.4
Au-198	0.111	0.623	0.18	0.0895	1.2

From Table 5.15, it is clear that for the given irradiation time, the nuclides with relatively long half-lives could not saturate, which led to the large errors in some of the nuclides for the analytical calculations. The MCNP results used in the manner given in Equation (35) can only be used to determine the saturated activity. For the isotopes that did saturate during the given irradiation time, the agreement between the analytical and simulated results is still weak. Figure 5.7 shows the simulated-to-analytical activity ratio if each of the nuclides were taken to saturation. There is no identifiable trend in the error and the average of the ratios is 0.83.

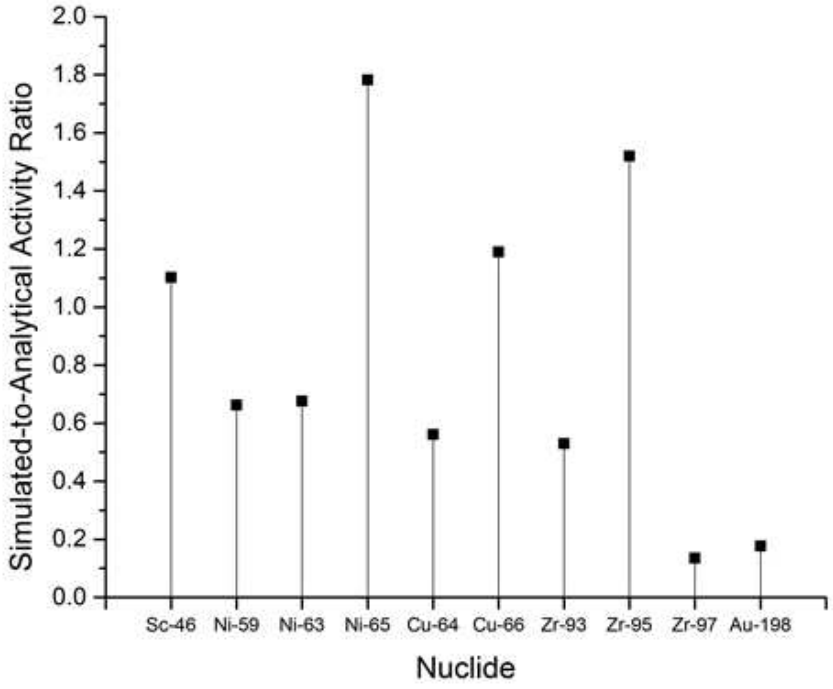

Figure 5.7. Activity Ratios between MCNP and Analytical Calculations

The simulated-to-induced ratios, plotted in Figure 5.8, are somewhat closer to the ideal value of 1 for most of the isotopes from which an activity measurement was obtained. The ratio from the Cu-64 values is the outlier of the group where the other ratios center around 1.4. The average of these ratios was found to be 1.28. The difference in values may be discovered in the way the spectroscopy system determines the activity, given by [42]:

$$A\ (\mu\text{Ci}) = \frac{\text{Net Area}}{(\text{Live time})(\text{Efficiency})(\text{Yield})(3.7\times10^{4})} \tag{39}$$

where the Net Area is obtained as the integral of the counts during a measurement session, the Live Time is the analog-to-digital converter live time that the spectroscopy system accounts for automatically, Efficiency is the ability of the detector to detect the

actual amount of gamma rays at a particular energy, Yield is the amount of gamma rays released per disintegration, and 3.7×10^4 is a conversion factor from Bq to μCi. The efficiency spectrum is calibrated by the user, which accounts for geometry, energy detection, and other factors. The errors between the MCNP and measured results could be explained by a non-ideal calibration curve that does not apply well to every gamma ray energy. Testing this hypothesis would require an additional foil irradiation time and a recalibrated spectroscopy system.

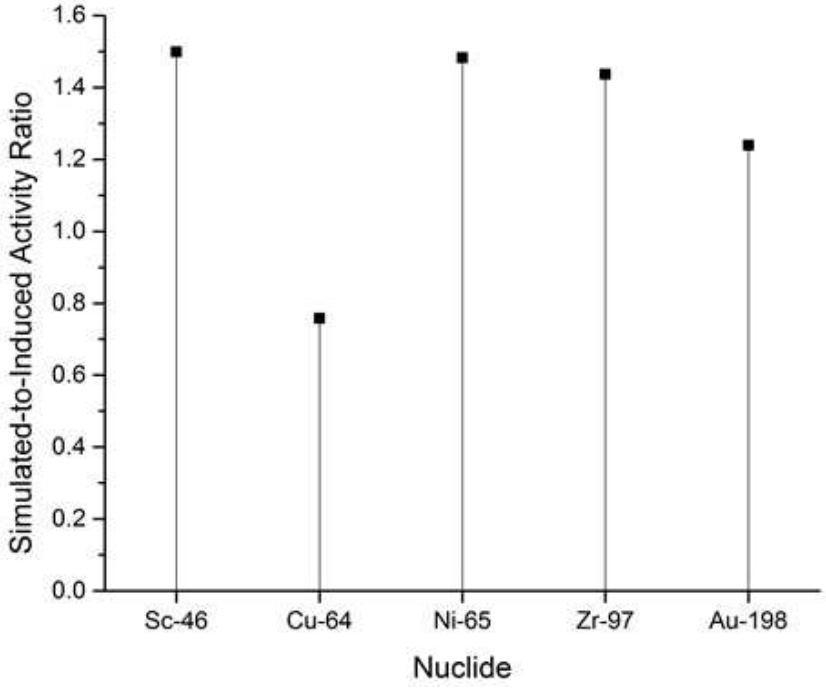

Figure 5.8. Activity Ratios between MCNP and Measured Values

6 SUMMARY AND FUTURE WORK

The results from the comparative analysis for each of the different radiation sources are summarized in this chapter. Explanations for the disagreements between the analytical and simulated results are also provided here.

- The photon fluence was described correctly by the theory in all cases. Deviations in value for the lateral device were attributed to the number of source particles simulated, which suggests that answers may not be accurate even if they pass all statistical checks with a low relative error.
- The theory which describes the photon energy deposition in a material tends to agree with MCNP with an error of less than 3% in the case of Co-60. The percent error was slightly higher in the case of the vertical devices, but this may be due to the significantly different number of points simulated.
- In the modified photon dose theory for ultraviolet radiation, where μ/ρ was used instead of μ_{en}/ρ, the results were within 2% of each other in the case of the lateral devices. The dose percent error was higher for the vertical device case when the ChG layer was photodoped.
- In both of the devices, the simulated 100 keV electron fluence was higher than the analytical fluence due to electron forward scattering. The same can be said for the 30 keV electron fluence. In the lateral devices, the electrons could not penetrate deep into the Si layer.
- The Katz-Penfold relation did not reliably predict the electron dose due to 100 keV or 30 keV electrons. There is clearly a material and a depth

dependence on the dose that the Katz-Penfold relation does not account for.

- For the neutron howitzer, both gamma ray and neutron dose rates were shown to be reliably modeled by MCNP. In the case of the neutrons, it is imperative to consider the geometry of the radiation counter along with the energy-dependent neutron quality factors.
- MCNP can be used to predict the maximum theoretical activity of a radiation foil, but the spectroscopy system must be calibrated correctly to allow a fair comparison. The percent difference of 50% shows that either the simulation or experimental values are incorrect, which indicates that more experimentation after recalibrating the spectroscopy system is needed.

In the case of the photon and electron simulations, it may be worthwhile to model the actual source geometry in the analysis of the ChG devices. Use of a monodirectional approximation was justified for each source, but researchers would be better informed in seeing how their devices operate under their particular radiation setup. It would also be fruitful for the Katz-Penfold relation to be researched in-depth and modified to fit MCNP dose results. This would make hand calculations more representative of the electron energy deposition that takes place as opposed to being an acceptable approximation within an order of magnitude. The generation constant plots can be updated if the optical gaps of more Ge-Se compositions are researched and if more concrete data on the ChG density dependence on Ag photodoping are obtained.

With the introduction of MCNP6.1 occurring relatively late into this research, many of its new capabilities could not be tested. Instead of defining the Cf-252 neutron energy spectrum using the Watt fission spectrum, MCNP6.1 can now automatically determine the neutron spectrum based on the isotopes detected within a cell. Using this function in the neutron howitzer simulation has the potential to produce even more accurate results. The UV simulations would need to be redone when low-energy photon physics is implemented more effectively in MCNP.

Finally, a recalibration to the spectroscopy system must be done and the activation foils irradiated again to better compare between the MCNP activity results and those obtained experimentally.

REFERENCES

[1] N. Metropolis, “The Beginning of the Monte Carlo Method,” Los Alamos National Laboratory, Los Alamos, NM, Tech. Rep. LA-UR-88-9067, 1987.

[2] D. Alloni et al., “Final characterization of the first critical configuration for the TRIGA Mark II reactor of the University of Pavia using the Monte Carlo code MCNP.” *Prog. in Nucl. Energy*, vol. 74, pp. 129-135, Feb. 2014.

[3] C. R. Hughes et al., “Multi-physics analysis of a supercritical water reactor with improved MCNP modeling.” *Nucl. Eng. Des.*, vol. 270, pp. 412-420, Jan. 2014.

[4] F. Carré and G. L. Fiorini. (2004, Apr. 21). Status of the Generation IV Initiative on Future Nuclear Energy Systems. [Online]. Available: http://www.euronuclear.org/1-information/generation-IV.htm.

[5] J. D. Wallace, “Monte Carlo modelling of large scale NORM sources using MCNP.” *J. Environ. Radioact.*, vol. 126, pp. 55-60, June 2013.

[6] J. Ghassoun, “Effect of tissue inhomogeneities on dose distributions from Cf-252 brachytherapy source.” *Appl. Radiat. Isot.*, vol. 71, pp. 1-6, Sept. 2012.

[7] P. Dandamudi, “Resistance switching in chalcogenide based programmable metallization cells (PMC) and sensors under gamma-rays,” Ph.D. dissertation, School of Elect. Comp. and En. Eng., Arizona State Univ, Tempe, AZ, 2013.

[8] X-5 Monte Carlo Team, “MCNP – A General Monte Carlo N-Particle Transport Code, Version 5. Volume I: Overview and Theory,” LANL, Los Alamos, NM, LA-UR-03-1987, Feb. 2008.

[9] J. H. Hubbell and S. M. Seltzer. (2004 July). *Tables of x-ray mass attenuation coefficients and mass-energy absorption coefficients from 1 keV to 20 MeV for elements Z = 1 to 92 and 48 additional substances of dosimetric interest* [Online]. Available: http://www.nist.gov/pml/data/xraycoef/index.cfm

[10] J. K. Shultis and R. E. Faw, “Radiation Interactions,” in *Fundamentals of Nuclear Science and Engineering*, second ed. Boca Raton, FL: Taylor and Francis Group, 2008, pp. 178-182.

[11] L. Katz and A. S. Penfold, “Range-energy relations for electrons and the determination of beta-ray end-point energies by absorption,” *Rev. of Mod. Phys.*, vol. 24, pp. 27-44, Jan. 1952.

[12] J. R. Lamarsh and A. J. Baratta, “Interaction of Radiation with Matter,” in *Introduction to Nuclear Engineering*, third ed. Upper Saddle River, NJ: Prentice-Hall Inc., 2001, pp. 52-53.

[13] A. Chandran, “Radiation sensing using chalcogenide glass materials,” M.S. thesis, School of Elect. Comp. and Elec. Eng., Arizona State Univ. Tempe, AZ, 2012.

[14] R. A. Dragoset et al. (2013, May). *Periodic Table: Atomic Properties of the Elements* [Online]. Available: http://www.nist.gov/pml/data/periodic.cfm

[15] D. E. Cullen et al., “EPDL97: The Evaluated Photon Data Library, ’97 Version,” UCRL-50400, vol. 6, rev. 5, Lawrence Livermore National Laboratory (1997).

[16] J. K. Shultis and R. E. Faw, “Radiation Interactions,” in *Fundamentals of Nuclear Science and Engineering*, second ed. Boca Raton, FL: Taylor and Francis Group, 2008, pp. 180.

[17] R. C. Alig and S. Bloom, “Electron-Hole-Pair Creation Energies in Semiconductors,” *Physical Review Letters*, vol. 35, pp. 1522-1525, Dec. 1975.

[18] P. Dandamudi, private communication, Jan. 2013.

[19] J. M. Conde Garrido et al., “Compositional dependence of the optical properties on amorphous $Ag_x(Ge_{0.25}Se_{0.75})_{100-x}$ thin films,” *J. Non-Cryst. Solids*, vol. 377, pp. 186-190, 2013.

[20] Y. Gonzalez-Velo, private communication, Dec. 2012.

[21] M. Kozicki, private communication, Oct. 2014.

[22] M. A. Popescu, “Physico-Chemical Properties of Chalcogens and Binary Chalcogenide Glasses,” in *Non-Crystalline Chalcogenides*, Dordrecht, The Netherlands: Springer Netherlands, 2000, pp. 184.

[23] J. Orava et al., “Optical and structural properties of Ge-Se bulk glasses and Ag-Ge-Se thin films,” *J. Non-Cryst. Solids*, vol. 355, pp. 1951-1954, 2009.

[24] M. I. Mitkova et al., “Morphology of electrochemically grown silver deposits on silver-saturated Ge-Se thin films,” *J. Non-Cryst. Solids*, vol. 326-327, pp. 425-429, 2003.

[25] D. B. Pelowitz et al., “MCNP6 User’s Manual, Version 1.0,” LANL, Los Alamos, NM, LA-CP-13-00634, May 2013.

[26] M. J. Berger et al. (2005 Aug.). *ESTAR, PSTAR, and ASTAR: Computer Programs for Calculating Stopping-Power and Range Tables for Electrons, Protons, and Helium Ions* (version 1.2.3) [Online]. Available: http://physics.nist.gov/Star

[27] National Institute of Standards and Technology. *ESTAR: Stopping-Power and Range Tables for Electrons* [Online]. Available: physics.nist.gov/PhysRefData/Star/Text/ESTAR.html

[28] W. C. Mosley et al., "Californium oxide – palladium cermet wire as a ^{252}Cf neutron source form," Savannah River Laboratory, Aiken, 1974.

[29] High Tech Sources Limited, "Californium-252," QSA Global, Didcot, 2013.

[30] V. Chisté et al., "Table of Radionuclides (Vol. 4 - A = 133 to 252)," Bureau International Des Poids Et Mesures, Sèvres, 2008.

[31] A. B. Smith et al., "Prompt Gamma Rays Accompanying the Spontaneous Fission of Cf252," *Phys. Rev.*, vol. 104, no. 3, pp. 699-702, 1956.

[32] T. E. Valentine, *Evaluation of Prompt Gamma Rays for Use in Simulating Nuclear Safeguard Measurements.* ORNL/TM/-1999/300. Oak Ridge Nat. Lab. Oak Ridge, TN. Oct 1999.

[33] V. V. Verbinski et al., "Prompt Gamma Rays from ^{235}U(n,f), ^{239}Pu(n,f), and Spontaneous Fission of ^{252}Cf," *Phys. Rev. C*, pp. 1173-1185, Mar. 1973.

[34] B. Becker et al., "Monte Carlo Hauser-Feshbach predictions of prompt fission γ rays: Application to n_{th} + ^{235}U, n_{th} + ^{239}Pu, and ^{252}Cf (sf)," *Phys. Rev. C*, vol. 87, pp. 014617, Jan. 2013.

[35] R. B. Hayes, "Preliminary Benchmarking Efforts and MCNP Simulation Results for Homeland Security," *Nuclear Technology*, vol. 168, no. 3, pp. 852-857, 2008.

[36] D. H. Stoddard, "Radiation Properties of Californium-252," USAEC Report DP-986, Savannah River Laboratory, Aiken, 1965.

[37] United States Nuclear Regulatory Commission. (2014, July 10). *NRC: 10 CFR 20.1004 Units of radiation dose* [Online]. Available: http://www.nrc.gov/reading-rm/doc-collections/cfr/part020/part020-1004.html.

[38] Ludlum Measurements, Inc., "Ludlum model 12-4 survey meter with He-3 neutron detector," April 2014. [Online]. Available: http://www.ludlums.com/images/stories/product_manuals/M12-4.pdf. [Accessed 16 July 2014].

[39] Oregon State University, "Oregon State TRIGA Reactor Operating Procedures," February 2010. [Online]. Available: http://radiationcenter.oregonstate.edu/sites/radiationcenter.oregonstate.edu/files/Documents/OSTROP18AppendixA%20rev%20LEU-2.pdf. [Accessed 14 May 2014].

[40] F. W. Walker et al. Chart of the Nuclides, 12th Ed. General Electric Company, Schenectady, NY, 1977.

[41] K. E. Holbert. Transmutation – EEE 460 Nuclear Power Engineering. Arizona State University. Tempe, USA. [Online]. Available: http://holbert.faculty.asu.edu/eee460/Transmutation.pdf.

[42] CANBERRA. Spectrum Analysis – Canberra Industries. [Online]. Available: http://users.df.uba.ar/sgil/labo5_uba/recursos/Spectrum%20Analysis%20-%20Canberra%20Industries.htm

APPENDIX A

MCNP INPUT DECK: NICKEL ACTIVATION FOIL IN HOWITZER

Cf-252 Source, Neutrons
c cell cards
1 1 -15.165 -100 101 -102 IMP:n,p=1 $ fuel capsule
2 2 -8.03 -103 104 -105 (1050:-1051:1052) IMP:n,p=1 $ steel casing
20 7 -12.02 -1050 1051 -1052 (100:-101:102) IMP:n,p=1 $ palladium casing
3 3 -0.001205 -108 106 -107 (103:-104:105) #6 1080 #133 &
#60 #61 IMP:n,p=1 $ air half
30 4 -0.92 -108 106 -107 -1080 1030 IMP:n,p=1 $ poly half
4 4 -0.92 106 -111 112 -113 114 -115 (108:107) &
1111 #111 #112 #113 #114 #115 #116 #117 #118 &
#129 #130 #131 #132 #45 IMP:n,p=1 $ inner around air
40 4 -0.92 1111 111 -1110 112 -113 114 -115 &
#129 #130 #131 #132 IMP:n,p=1 $ inner box above
41 3 -0.001205 1111 1110 -11100 112 -113 114 -115 &
#129 #130 #131 #132 IMP:n,p=1 $ air gap above
42 5 -0.95 -1111 107 -111 125 126 IMP:n,p=1 $ b-poly above air
43 4 -0.92 116 -106 112 -113 114 -115 125 &
#111 #112 #113 #114 #115 #116 #117 #118 &
#129 #130 #131 #132 #45 IMP:n,p=1 $ poly below air
44 4 -0.92 110 -116 112 -113 114 -115 &
(1111:-110:116) #111 #112 #113 #129 #130 #131 #132 IMP:n,p=1 $ under of tray
440 5 -0.95 -1111 110 -116 125 IMP:n,p=1 $ b-poly under tray
45 3 -0.001205 1141 -1142 1143 -107 114 -1140 IMP:n,p=1 $ air in cover
c 500 5 -0.95 -1211 116 (-112:113:-114:115)
5 5 -0.95 (11100:-112:113:-114:115) 125 126 &
116 -1170 118 -119 120 -121 &
#100 #101 #102 #103 #104 #105 #106 #107 #108 #109 #110 &
#119 #120 #121 #122 #123 #124 #125 #126 #127 #128 IMP:n,p=1 $ outer box
50 5 -0.95 1170 -117 1180 -1190 1200 -1210 125 126 &
#107 #108 #109 #110 IMP:n,p=1 $ outer box, lid
51 5 -0.95 -1111 -11100 111 125 126 IMP:n,p=1 $ b-poly tube in mid
52 5 -0.95 -1111 117 -1171 #98 #96 #135 IMP:n,p=1 $ b-poly tube on top
53 3 -0.001205 116 -1211 112 -113 1201 -120 IMP:n,p=1 $ door
c 52 5 -0.95 -1111 117 -1171 (125:128) #97 IMP:n,p=1 $ b-poly tube on top
6 9 -8.908 -1220 -1221 1223 IMP:n,p=1 $ foil
60 10 -0.207 1220 -12200 -12201 12202 IMP:n,p=1 $ vinyl holder
61 10 -0.207 -12203 12204 12205 -12206 #60 &
12207 12208 IMP:n,p=1 $ vinyl holder for vinyl
7 6 -1 -123 IMP:n,p=1 $ outer bubble
70 6 -1 -1230 IMP:n,p=1 $ upper bubble
80 3 -0.001205 -124 -116 (-112:113:-114:115:-110) IMP:n,p=1 $ air below poly
81 3 -0.001205 -124 1230 117 (1111:1171) &
IMP:n,p=1 $ air around/above cyl on top
82 3 -0.001205 -124 -117 1170 (-1180:1190:-1200:1210) &
IMP:n,p=1 $ air around lid

```
83 3 -0.001205 -124 -1170 116 120 (-118:119:121) &
IMP:n,p=1 $ air around mid
830 3 -0.001205 -124 123 -1201 -1170 116 IMP:n,p=1 $ air in front of door
831 3 -0.001205 -124 -1170 116 -120 1201 #53 IMP:n,p=1 $ air around door
90 3 -0.001205 -125 110 -116 IMP:n,p=1 $ track, bottom b-poly
91 3 -0.001205 -125 116 -106 IMP:n,p=1 $ track, tray
92 3 -0.001205 -125 107 -111 #133 IMP:n,p=1 $ track, b-poly above air
920 3 -0.001205 -126 107 -111 IMP:n,p=1 $ ltrack, b-poly above air
93 3 -0.001205 -125 111 -11100 #133 #134 IMP:n,p=1 $ track, b-poly to outer
930 3 -0.001205 -126 111 -11100 IMP:n,p=1 $ track, ltrack, b-poly to outer
94 3 -0.001205 -125 11100 -1170 #134 #135 IMP:n,p=1 $ track, outer to lid
940 3 -0.001205 -126 11100 -1170 IMP:n,p=1 $ ltrack, outer to lid
95 3 -0.001205 -125 1170 -117 #135 IMP:n,p=1 $ track, lid to upper cyl
950 3 -0.001205 -126 1170 -117 IMP:n,p=1 $ ltrack, lid to upper cyl
c 96 3 -0.001205 -125 117 -128 IMP:n,p=1 $ track, inside upper cyl
c 97 3 -0.001205 -127 -1111 130 IMP:n,p=1 $ track, upper cyl exit
96 3 -0.001205 117 (-126:-127) 1300 -128 -1111 -1171 &
IMP:n,p=1 $ leads track in cyl
98 3 -0.001205 117 (-125:-127) -130 -128 -1111 -1171 #135 &
IMP:n,p=1 $ source track in cyl
100 8 -2.70 -131 1310 -1170 IMP:n,p=1 $ bolts in lid
101 8 -2.70 -132 1310 -1170 IMP:n,p=1
102 8 -2.70 -133 1310 -1170 IMP:n,p=1
103 8 -2.70 -134 1310 -1170 IMP:n,p=1
104 8 -2.70 -139 1310 -1170 IMP:n,p=1
105 8 -2.70 -140 1310 -1170 IMP:n,p=1
106 8 -2.70 -141 1310 -1170 IMP:n,p=1
107 8 -2.70 -135 1310 -117 IMP:n,p=1
108 8 -2.70 -136 1310 -117 IMP:n,p=1
109 8 -2.70 -137 1310 -117 IMP:n,p=1
110 8 -2.70 -138 1310 -117 IMP:n,p=1
111 8 -2.70 -142 110 -111 IMP:n,p=1 $ bolts on rot. table
112 8 -2.70 -143 110 -111 IMP:n,p=1
113 8 -2.70 -144 110 -111 IMP:n,p=1
114 8 -2.70 -145 106 -107 IMP:n,p=1 $ bolts on tray
115 8 -2.70 -146 106 -107 IMP:n,p=1
116 8 -2.70 -147 106 -107 IMP:n,p=1
117 8 -2.70 -161 106 -107 IMP:n,p=1 $ bolts on tray cover
118 8 -2.70 -162 106 -107 IMP:n,p=1
119 8 -2.70 -148 118 -112 IMP:n,p=1 $ bolts on outer box
120 8 -2.70 -149 118 -112 IMP:n,p=1
121 8 -2.70 -148 113 -119 IMP:n,p=1
122 8 -2.70 -149 113 -119 IMP:n,p=1
123 8 -2.70 -150 115 -121 IMP:n,p=1
124 8 -2.70 -151 115 -121 IMP:n,p=1
```

```
125 8 -2.70 -152 120 -114 IMP:n,p=1
126 8 -2.70 -153 120 -114 IMP:n,p=1
127 8 -2.70 -154 120 -114 IMP:n,p=1
128 8 -2.70 -155 120 -114 IMP:n,p=1
129 8 -2.70 -156 110 -160 IMP:n,p=1 $ fasteners
130 8 -2.70 -157 110 -160 IMP:n,p=1
131 8 -2.70 -158 110 -160 IMP:n,p=1
132 8 -2.70 -159 110 -160 IMP:n,p=1
133 8 -2.70 -103 105 -163 IMP:n,p=1 $ Al holding onto source
134 2 -8.03 -164 163 -165 IMP:n,p=1 $ 1st sect steel
135 2 -8.03 -164 165 -166 IMP:n,p=1 $ 2nd sect steel
200 3 -0.001205 106 -107 -1030 -1080 #1 #2 #20 #133 IMP:n,p=1 $ source channel
999 0 124 IMP:n,p=0 $ Void outside sphere

c surface cards
c Cf-252 source
100 C/Y -1.27 0 0.0780391759 $ Cf-252
101 py 0.92
102 py 1.62
103 C/Y -1.27 0 0.47625 $ Steel casing
104 py -0.3175
105 py 2.8575
1050 C/Y -1.27 0 0.0785391759 $ arbitrary palladium casing
1051 py 0.9195
1052 py 1.6205
1030 C/Y -1.27 0 0.47625001
c Air chamber
106 py -3.175 $ bottom of air chamber
107 py 5.715 $ top of chamber
108 cy 12.065 $ radius of air chamber
1080 pz 0 $ division between air/poly halves
c inner box
110 py -19.685 $ very bottom of poly
111 py 10.795 $ poly above chamber
1110 py 26.035 $ start of air gap
11100 py 29.845 $ end of air gap
1111 C/Y 0 0 5.08 $ tube of b-poly
112 px -20.32 $ left side of poly
113 px 20.32 $ right side of poly
114 pz -20.32 $ depth of poly, neg
1140 pz -19.685 $ poly cover missing
1141 px -18.415 $ left side of poly cover missing
1142 px 18.415 $ right side of poly cover missing
1143 py -4.445 $ bottom of poly cover missing
115 pz 20.32 $ depth of poly, pos
```

```
c outer box
116 py -5.715 $ bottom of outer shield
117 py 40.005 $ top of outer shield
1170 py 34.925 $ start of upper lid
1171 py 54.505 $ end of upper cylinder
118 px -30.75 $ outer left bound
1180 px -25.98 $ inner left bound
119 px 30.75 $ outer right bound
1190 px 25.98 $ inner right bound
120 pz -30.75 $ depth bound, neg outside
1200 pz -25.98 $ depth bound, neg inside
1201 pz -31.385 $ door being too thick
121 pz 30.75 $ depth bound, pos outside
1210 pz 25.98 $ depth bound, pos inside
1211 py 24.385 $ top of bottom shield
c test bubbles
c 122 s -1.27 1.27 6.35 1 $ sample
1220 c/z -1.27 1.27 0.635 $ foil
1221 pz 6.3627
1223 pz 6.3373
12200 c/z -1.27 1.27 0.79375 $ (outer) cyl of vinyl
12201 pz 6.588125
12202 pz 6.111875
12203 c/y -1.27 6.35 1.11125 $ (outer) holder cyl of vinyl
12204 c/y -1.27 6.35 0.79375 $ (inner)
12207 c/x 1.27 7.62 1.031875
12208 c/x 1.27 5.08 1.031875
12205 py -2.2225
12206 py 2.8575
123 s -1.27 1.27 -42.18 1.5 $ on side
1230 s 16.51 51.435 0 1.5 $ on top
124 so 400 $ world sphere
c air tracks
125 C/Y -1.27 0 0.5969 $ source guiding track
126 C/Y 1.27 0 0.5969 $ leads guiding track
c 127 C/X 45.085 0.5969 0.5969 $ horizontal, exit
127 C/X 45.085 0 0.5969 $ horizontal, exit
128 py 45.6819000001 $ top of track
c 128 py 45.085 $ top of track
130 px -0.673099 $ right edge of source exit
1300 px 0.673099 $ left edge of leads exit
c ////////////////////
c ////////////////////
c aluminum cylinders; bolts and fasteners
c on lid
```

```
1310 py 24.765 $ bottom of lid's bolts
131 C/Y -27.48 27.48 0.3175 $ 0
132 C/Y -27.48 -27.48 0.3175 $ 1
133 C/Y 27.48 -27.48 0.3175 $ 2
134 C/Y 27.48 27.48 0.3175 $ 3
135 C/Y -23.28 0 0.3175 $ 4
136 C/Y 0 -23.48 0.3175 $ 5
137 C/Y 23.48 0 0.3175 $ 6
138 C/Y 0 23.48 0.3175 $ 7
139 C/Y -17.68 27.48 0.3175 $ 8
140 C/Y -17.68 -27.48 0.3175 $ 9
141 C/Y 27.48 17.68 0.3175 $ 10
c on rotation table
142 C/Y 0 -15.24 0.3175 $ 0
143 C/Y 15.24 -2.54 0.3175 $ 1
144 C/Y -15.24 -2.54 0.3175 $ 2
c on tray
145 C/Y 0 15.24 0.3175 $ 0'
146 C/Y 15.24 2.54 0.3175 $ 1'
147 C/Y -15.24 2.54 0.3175 $ 2'
c on outer box
148 C/X 9.485 15.24 0.3175 $ 0,2
149 C/X 9.485 -15.24 0.3175 $ 1,3
150 C/Z -12.7 9.525 0.3175 $ 4
151 C/Z 12.7 9.525 0.3175 $ 5
152 C/Z -16.08 -0.635 0.3175 $ 6
153 C/Z 16.08 -0.635 0.3175 $ 7
154 C/Z 16.08 16.585 0.3175 $ 8
155 C/Z -16.08 16.585 0.3175 $ 9
c fastener
156 C/Y 19.82 19.82 0.15875
157 C/Y 19.82 -19.82 0.15875
158 C/Y -19.82 -19.82 0.15875
159 C/Y -19.82 19.82 0.15875
160 py 29.21 $ top of rods
c on tray cover
161 C/Y 17.32 17.32 0.3175
162 C/Y -17.32 17.32 0.3175
c cable parts
163 py 14.2875 $ top of aluminum part
c steel cable
164 C/Y -1.27 0 0.15875 $ Steel casing
165 py 33.3375 $ top of chain, 8in from Al
166 py 44.4119 $ furthest chain goes
```

```
c data cards
SDEF POS=-1.27 1.27 0 CEL=1 ERG=d1 RAD=d2 EXT=D3 AXS=0 1 0 PAR=1
c SDEF POS=-1.27 2.54 0 CEL=1 ERG=d1 PAR=1
SP1 -3 1.025 2.926
SI2 0 0.476250001
SP2 -21 0
SI3 -0.30 2.9
SP3 -21 0
mode N P
m1  98252 -6.220868941e-4 $ Cf-252
  98251 -3.149807059e-5
  98250 -1.181177647e-4
  98249 -1.574903529e-5
  46102 -0.0101919201 $ palladium
  46104 -0.1113117549
  46105 -0.2231231137
  46106 -0.2730835064
  46108 -0.2643903981
  46110 -0.1171071604
  8016 -4.694664845e-6
m2  6012 -0.079144 $ stainless steel, C
  6013 -8.56e-4
c  25000 -2 $ Mn
c  15000 -0.045 $ P
  16032 -0.028479
  16033 -0.000228
  16034 -.001287
  16036 -6e-6
  14028 -0.6916725
  14029 -0.0351375
  14030 -0.02319
  24050 -0.7821 $ Cr
  24052 -15.08202 $ Cr
  24053 -1.71018 $ Cr
  24054 -0.4257 $ Cr
  28058 -5.446152 $ Ni
  28060 -2.987848 $ Ni
  28061 -0.091192 $ Ni
  28062 -.29076 $ Ni
  28064 -0.074048 $ Ni
c  7000 -0.10 $ N
  26054 -4.15900975 $ Fe
  26056 -64.2875587 $ Fe
  26057 -1.50777445 $ Fe
  26058 -0.2006571 $ Fe
```

```
m3  7014 -76.8 $ air
  8016 -23.2
m4  1001 -14.36834745 $ pure polyethylene
  1002 -0.00165255
  6012 -84.713759
  6013 -0.916241
m5  1001 -11.598666 $ boron-doped poly
  1002 -0.001334
  6012 -60.54516
  6013 -0.65484
  8016 -22.20
  5010 -0.995
  5011 -4.005
m6  1001 1.999977 $ water
  1002 2.3e-4
  8016 1
m7  46102 1.02 $ palladium
  46104 11.14
  46105 22.33
  46106 27.33
  46108 26.46
  46110 11.72
m8  13027 100 $ aluminum
m9  28058 68.077 $ Nickel
  28060 26.223
  28061 1.140
  28062 3.6345
  28064 0.9255
m10  6012 1.9786 $ C2H3, vinyl
  6013 0.0214
  1001 2.999655
  1002 3.45e-4
f04:n 6
f04m:n 6.222e-2 9 102
f14:n 6
f14m:n 3.322e-3 9 102
f24:n 6
f24m:n 8.460e-4 9 102
f34:n 6
f06:n 6
c f34:p 6
c E34 1e-3 0.01 0.1 1 10
c f36:p 6
c E36 1e-3 0.01 0.1 1 10
c f44:p 7
```

```
c E44 1e-3 0.01 0.1 1 10
c f46:p 7
c E46 1e-3 0.01 0.1 1 10
c f54:p 70
c E54 1e-3 0.01 0.1 1 10
c f56:p 70
c E56 1e-3 0.01 0.1 1 10
nps 15e6
```